FERMILAB-Pub-xx/yyy-T
June, 2013

Muon Collider Higgs Factory for Snowmass 2013

David B. Cline[(1)], Alex Conway[(7)], Mary Anne Cummings[(2)], V. Di Benedetto[(5)], Tao Han[(3)], Gail Hanson [(4)], Estia Eichten[(5)], Jack Gunion[(6)], Christopher T. Hill[(5)], Ron Lipton[(5)], Zhen Liu [3], Anna Mazzacane[(5)], Nikolai Mokhov[(5)], David Neuffer[(5)], Mark Palmer[(5)], Arvind Rajaraman, Don Summers, Nikolai Terentiev, Hans Wenzel[5],

(1) *University of California, Los Angeles, California;*
(2) *Muons Inc., Batavia, Illinois, 60510*
(3) *University of Pittsburgh, Pittsburgh, Pennsylvania;*
(4) *University of California, Riverside, California;*
(5) *Fermilab, P.O. Box 500, Batavia, Illinois, 60510;*
(6) *University of California, Davis, California;*
(7) *University of Chicago, Chicago, Illinois;*

Executive Summary

We propose the construction of a compact Muon Collider s-channel Higgs Factory. A Muon Collider Higgs Factory is part of an evolutionary program beginning with R&D on Muon Cooling with a possible neutrino factory such as νSTORM, the construction of Project-X with a rich program of precision physics addressing the $\sim$ 100 TeV scale, potentially leading ultimately to the construction of an energy frontier Muon Collider with μ^+ and μ^- colliding up to $\sim$ 10.0 TeV center-of-mass energy....

The Muon Collider Higgs Factory would utilize an intense proton beam from Project-X

Contents

1 Introduction

The discovery last year of a $J^{PC} = 0^{++}$ particle with a mass of 126 GeV [1] is most likely that of a Higgs boson, as anticipated by Weinberg in the original incarnation of the standard model [2]. The Higgs boson "accomodates" the masses of quarks, leptons and electroweak gauge bosons seen in nature. However, the origin of the Higgs-Yukawa coupling constants and mixing angles, as well as the origin of the Higgs boson mass itself, remain a mystery. The most important issues facing modern High Energy Physics are, therefore, to fully understand the the origin of electroweak symmetry breaking and to probe for any associated new physics at the electroweak scale.

New physics can potentially be revealed in detailed studies of Higgs boson parameters, such as the mass, decay widths and production amplitudes. Indeed, the LHC will go a long way toward revealing these detailed properties. New physics may also be discovered at higher energy scales indirectly, *e.g.*, through precision experiments at the "Intensity Frontier," such as through rare kaon decays, electric dipole moment searches, and probes of charged lepton and neutrino flavor physics. This is the purpose of "Project-X" in the near term at Fermilab. However, it is also important that the field continue to evolve along the path toward the direct probes of new physics, *i.e.*, at the "Energy Frontier." This demands a cost effective, and upward scaleable (in energy) strategy toward a program that can shed further light on the questions of electroweak physics and detailed properties Higgs Boson.

An attractive option along this path is the development of an s-channel Higgs factory using muons in a compact circular collider, *i.e.*, a "Muon Collider Higgs Factory." The muon has a Higgs-Yukawa coupling constant that enables direct s-channel production of the standard model Higgs boson at an appreciable rate. With an attainable, very small beam energy resolution of order ~ 4 MeV, operating at an energy of $m_H/2 = 62.5$ GeV and at a nominal luminosity of about $\sim 10^{32}$ cm^{-2} sec^{-1} such a collider would produce $40,000$ Higgs bosons per year. It affords precise observation of the mass and width of the Higgs boson by direct scanning, and the most precise determination of a Higgs-Yukawa couplng constant, that of the muon itself.

Since the muon is about 200 times heavier than an electron, synchrotron radiation from muon beams in a small radius circular machine is dramatically suppressed. This allows a muon collider facility to be much smaller than an e^+e^- facility at the same center-of-mass energy. The machine we are describing presently is detailed by Neuffer [**?**]

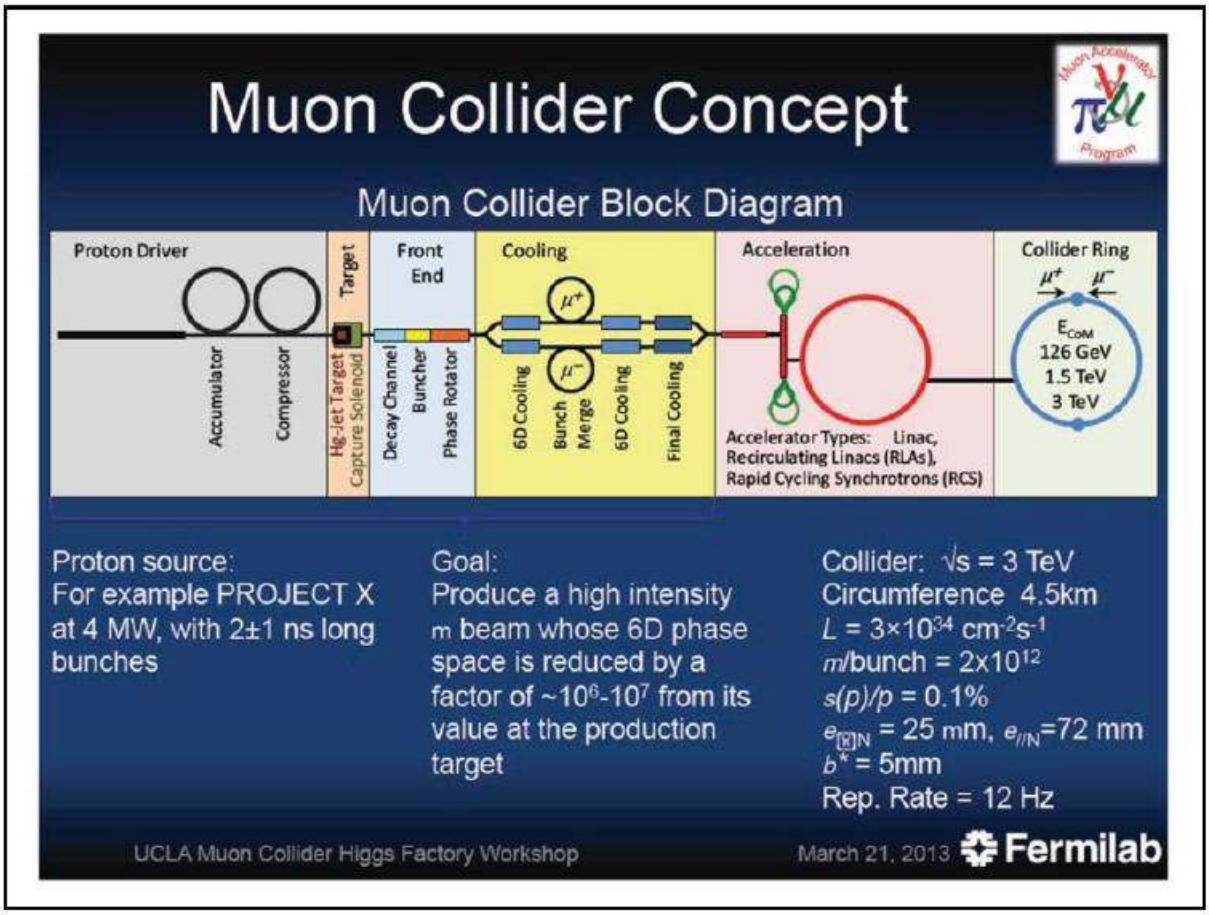

Figure 1: Muon Collider Higgs Factory schematic

and involves a collider storage ring of approximately 100 meters in diameter, roughly the size of the Fermilab Booster. The Muon Collider also provides superb energy resolution.

A conceptual design for a Muon Collider Higgs Factory facility is shown in Fig. 1. It consists of a source of short high-intensity proton pulses, a production target with collection of secondary π-mesons, followed by a decay channel. The produced $\mu^{\pm}$'s are collected and enter a bunching and cooling channel. Narrow intense muon pulses are then accelerated. Using clever sequencing and timing, the separate μ^- and μ^+ bunches can be accelerated in the same Project-X linac that produces the original intense proton source. The accelerated bunches are injected into the collider storage ring for collisions within an interaction region inside a detector.

The parameters for a Muon Collider Higgs Factory are given in Table 1 [4]. The

Parameter	Unit	Baseline	Upgrade
Beam energy	GeV	63	63
Average luminosity	$10^{31}/cm^2/s$	1.7	8.0
Collision energy spread	MeV	3	4
Circumference, C	m	300	300
Number of IPs	-	1	1
β^*	cm	3.3	1.7
Number of muons / bunch	10^{12}	2	4
Number of bunches / beam	-	1	1
Beam energy spread	%	0.003	0.004
Normalized emittance, $\varepsilon_{\perp N}$	π•mm•rad	0.4	0.2
Longitudinal emittance, $\varepsilon_{\|\|N}$	π•mm	1.0	1.5
Bunch length, σ_s	cm	5.6	6.3
Beam size at IP, r.m.s.	mm	0.15	0.075
Beam size in IR quads, r.m.s.	cm	4	4
Beam-beam parameter	-	0.005	0.02
Repetition rate	Hz	30	15
Proton driver power	MW	4	4

Table 1: Parameters of a $\mu^+\mu^-$ Collider at 126 GeV center-of-mass energy.

baseline design is shown, as well as an upgrade with transverse emittance reduced by additional cooling and β^* reduced by stronger focusing. focusing. The lattice for the baseline design is shown in Fig.2. With these parameters, luminosities of 1.7 to 8.0 $\times 10^{31}$ $cm^{-2}sec^{-1}$ can be achieved, giving 4,000 to 40,000 Higgs bosons per year.

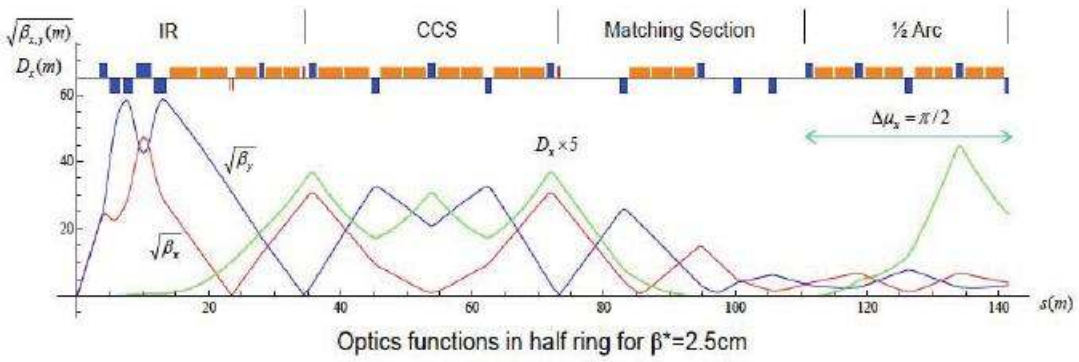

Figure 2: Muon Collider Higgs Factory lattice.

2 Physics at a Muon Collider Higgs Factory

A Muon Collider Higgs Factory has the following *a priori* advantages for physics:

- Small beam energy resolution (SBER) $\delta E/E \lesssim$ (few) $\times 10^{-5}$, allowing the study of direct s-channel production and a line-shape scan of the Higgs boson, as well as other heavier Higgs bosons as in multi-Higgs models.

- The s-channel Higgs production affords the most precise measurement of a second generation fermion Higgs-Yukawa coupling constant, the muon coupling, g_μ, to a precision $\delta g_\mu/g_\mu \sim$ (few)%. It allows the measurement of the renormalization group running of $g_\mu(q^2)$ from $q^2 = 0$ to $q^2 = m_h^2$. [**?**].

- The s-channel Higgs production affords the *best mass measurement of the Higgs boson* to a precision of $\sim$ (few) $\times 10^{-6}$ with a luminosity of $\mathcal{L} \sim 10^{32}$ cm^{-2}sec^{-1}.

- It affords the best direct measurement of the Higgs boson width to a precision of $\sim$ few% with a luminosity of $\mathcal{L} \sim 10^{33}$ cm^{-2}sec^{-1}; see Fig. 1, [**?**].

- This would yield the precise measurement of Higgs branching ratios to WW^* ZZ^* and $b\bar{b}$.

- At a upgraded luminosity of $\mathcal{L} \sim 10^{33}$ cm^{-2}sec^{-1} and ~ 3 "snowmass years" on the Z-pole, we would produce $\sim 10^9$ Z-bosons, the Higgs Factory permits a "Giga-Z program."

Detailed studies of these and other issues are underway, including: (1) optimal search strategy for the Higgs peak establishing a threshold integrated luminosity for physics of about $\sim$ (few) $\times 10^{31}$ cm^{-2}sec^{-1} [9, 10] ; (2) charm decay mode $h \to c\bar{c}$ appears to be accessible at a level of $\sim 8\sigma$ [11] ; (3) possible observable interference effects in *e.g.*, $h \to WW^*$.

2.1 Higgs Boson Signal and Background

One of the most appealing features of a muon collider Higgs factory is its s-channel resonant production of Higgs boson. For the production $\mu^+\mu^- \to h$ and a subsequent decay to a final state X with a $\mu^+\mu^-$ (partonic) c.m. energy $\sqrt{\hat{s}}$, the Breit-Wigner resonance reads

$$\sigma(\mu^+\mu^- \to h \to X) = \frac{4\pi\Gamma_h^2 \mathrm{Br}(h \to \mu^+\mu^-)\mathrm{Br}(h \to X)}{(\hat{s} - m_h^2)^2 + \Gamma_h^2 m_h^2}, \tag{2.1}$$

At a given energy, the cross section is governed by three parameters: m_h for the signal peak position, Γ_h for the line shape profile, and the product $B \equiv \mathrm{Br}(h \to \mu^+\mu^-)\mathrm{Br}(h \to X)$ for the overall event rate.

In reality, the observable cross section is given by the convolution of the energy distribution delivered by the collider. Assume that the $\mu^+\mu^-$ collider c.m. energy ($\sqrt{s}$) has a luminosity distribution

$$\frac{dL(\sqrt{s})}{d\sqrt{\hat{s}}} = \frac{1}{\sqrt{2\pi}\Delta} \exp[\frac{-(\sqrt{\hat{s}} - \sqrt{s})^2}{2\Delta^2}],$$

with a Gaussian energy spread $\Delta = R\sqrt{s}/\sqrt{2}$, where R is the percentage beam energy resolution; then, the effective cross section is

$$\sigma_{\mathrm{eff}}(s) = \int d\sqrt{\hat{s}}\ \frac{dL(\sqrt{s})}{d\sqrt{\hat{s}}} \sigma(\mu^+\mu^- \to h \to X) \tag{2.2}$$

An excellent beam energy resolution for a muon collider would make a direct determination of the Higgs boson width possible in contrast to the situations in the LHC and ILC. We first calculate the effective cross sections at the peak for the two different energy resolutions $R = 0.01\%$ and $R = 0.003\%$. We further evaluate the signal and SM background for the leading channels, $h \to b\bar{b},\ WW^*$.

We impose a polar angle acceptance for the final-state particles, $10^\circ < \theta < 170^\circ$. We assume a 60% single b-tagging efficiency and require at least one tagged b jet for the $b\bar{b}$

R (%)	$\mu^+\mu^- \to h$	$h \to b\bar{b}$		$h \to WW^*$	
	σ_{eff} (pb)	σ_{Sig}	σ_{Bkg}	σ_{Sig}	σ_{Bkg}
0.01	16	7.6	15	3.7	0.051
0.003	38	18		5.5	

Table 2: Effective cross sections (in pb) at the resonance $\sqrt{s} = m_h$ for two choices of beam energy resolutions R and two leading decay channels, with the SM Higgs branching fractions $\text{Br}_{b\bar{b}} = 56\%$ and $\text{Br}_{WW^*} = 23\%$ [7]. This table is taken from Ref [8].

final state. The backgrounds are assumed to be flat with cross sections evaluated right at 126 GeV using Madgraph5 [6].

We tabulate the results in Table 2. The background rate of $\mu^+\mu^- \to Z^*/\gamma^* \to b\bar{b}$ is 15 pb, and the rate of $\mu^+\mu^- \to WW^* \to 4$ fermions is only 51 fb, as shown in Table 2. Here, we consider all the decay modes of WW^* because of its clear signature at a muon collider. The four-fermion backgrounds from $Z\gamma^*$ and $\gamma^*\gamma^*$ are smaller to begin with and can be greatly reduced by kinematical considerations such as by requiring the invariant mass of one pair of jets to be near m_W and setting a lower cut for the invariant mass of the other pair.

2.2 Finding the Mass Window of the Higgs Boson

It is expected that the Higgs mass will be known to better than 100 MeV from measurements at the LHC (or ILC). However the natural width of a 126 GeV Higgs is only 4.2 MeV, so the first task for a muon collider is to rediscovery the Higgs Boson. After the Higgs has been located the full power of a Muon Collider tuned to sit on the peak of the Higgs resonance can be employed to study Higgs physics.

Alex Conway, Hans Wenzel [9] and Estia Eichten [10] have studied the optimum strategy to find the Higgs at a Muon Collider. They studied the required total luminosity to observe a 5σ (3σ) Higgs boson signal with various likelihoods and energy steps. It was assumed that a energy resolution of $4MeV$ is obtainable at a Muon Collider.

Two decay channels were considered: (1) the $b\bar{b}$ final state and (2) the WW^* final state. The $b\bar{b}$ final state has the largest branching fraction but has a significant background even for the excellent energy spread possible at the muon collider. The WW^* channel has very small background physics rates (two orders of magnitude smaller than the Higgs signal). For this study all the full WW^* decay rate is used.

The best strategy was found to use energy steps equal to the beam spread with

Channel	σ_{sig} (pb) σ_{bkgr} (pb)	Luminosity Required (pb^{-1})	
		$CL = 3\sigma$	$CL = 5\sigma$
Total	$\sigma_s = 28.3$ $\sigma_b = 301.4$	1,723	3,840
Total (Cut)	$\sigma_s = 22.4$ $\sigma_b = 126.4$	1,193	2,666
$b\bar{b}$	$\sigma_s = 16.5$ $\sigma_b = 57.2$	1,033	2,317
$b\bar{b}$ (Cut)	$\sigma_s = 8.64$ $\sigma_b = 8.45$	697	1,593
WW^*	$\sigma_s = 6.39$ $\sigma_b = 0.05$	146	389
WW^* (Cut)	$\sigma_s = 3.35$ $\sigma_b = 0.05$	325	812
$b\bar{b},\ WW^*$	$\sigma_s = --$ $\sigma_b = --$	105	368

Table 3: Required luminosity to guarantee finding a 5σ Higgs signal with confidence level $p = 3\sigma, 5\sigma$ [9].

the choice of the next energy bin determined by the maximum probability of discovery weighted by the prior of the LHC measurements. The WW^* channel is the most effective but both channels are included in the final results. The results for the combined channels from Conway and Wenzel [9] is shown in Table 3 for various p-values of non-discovery.

It is clear from Table 3 that reducing the error on the LHC determination of the mass of the Higgs could greatly aid finding the Higgs resonance at a Muon Collider.

2.3 Precision on Total Width

Higgs boson's total decay width (Γ_h) is to a very large extent of the most fundamental importance in all of the Higgs boson properties. It determines the overall coupling strength. Once the total width is known, the partial decay widths to different channels would be readily available and thus model-independent couplings strength can be derived.

We first generate pseudo-data in accordance with a Breit-Wigner resonance at 126 GeV convoluted with the beam energy profile integrated over $\sqrt{\hat{s}}$. These data are then randomized with a Gaussian fluctuation with variance the total number of events expected, including both signal and background. The results for the leading two channels $b\bar{b}$ and WW^* are shown in Fig. 3 for different integrated luminosities and beam energy resolu-

tions.

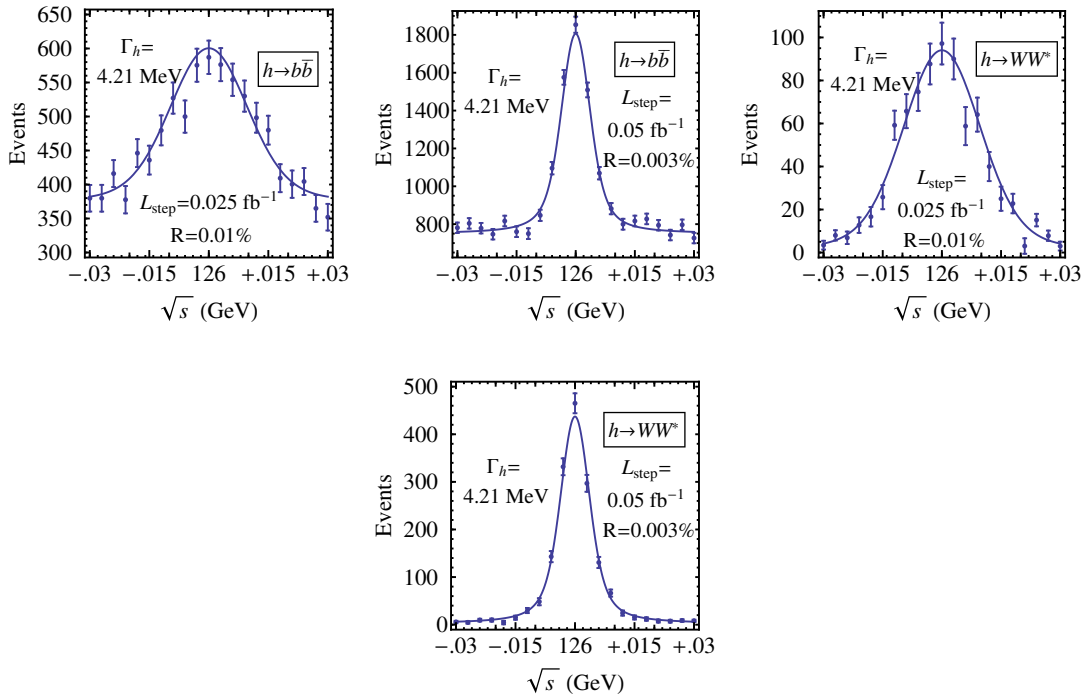

Figure 3: Number of events of the Higgs signal plus backgrounds and statistical errors expected for two different beam energy resolutions and integrated luminosities as a function of the collider energy $\sqrt{s}$ in $b\bar{b}$ and WW^* final states with a SM Higgs $m_h = 126$ GeV and $\Gamma_h = 4.21$ MeV. The detector background are not included, see more discussion in Sec.xx.(**refer to section discussing machine background**). These figures are taken from Ref [8].

We adopt a χ^2 fit over the scanning points with three model-independent free parameters in the theory Γ_h, B and m_h as mentioned in Eq. 2.1. To see the effects from the available luminosity, we show our results for the SM Higgs width determination in Fig. 4 for both resolutions by varying the luminosity. The achievable accuracies with the 20-step scanning scheme by combining two leading channels are summarized in Table 4 for three representative luminosities per step.

The mass and cross section can be simultaneously determined along with the Higgs width to a high precision. The results obtained are largely free from theoretical uncertainties. The major systematic uncertainty comes from our knowledge of beam properties [3]. The uncertainty associated with the beam energy resolution R will directly add to our statistical uncertainties of Higgs width. This uncertainty can be calibrated by

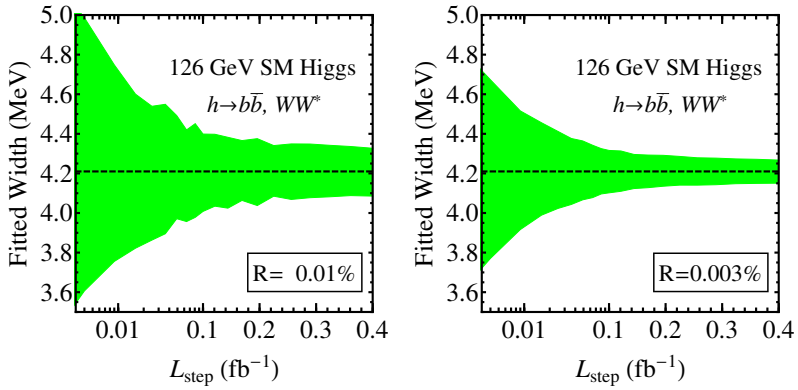

Figure 4: Fitted values and errors for the SM Higgs width versus the luminosity per step with the 20-step scanning scheme with 3-MeV step size. These figures are taken from Ref [8].

$\Gamma_h = 4.21$ MeV	$L_{\rm step}$ (fb^{-1})	$\delta\Gamma_h$ (MeV)	δB	δm_h (MeV)
$R = 0.01\%$	0.005	0.73	6.5%	0.25
	0.025	**0.35**	**3.0%**	**0.12**
	0.2	0.17	1.1%	0.06
$R = 0.003\%$	0.01	0.30	4.4%	0.12
	0.05	**0.15**	**2.0%**	**0.06**
	0.2	0.08	1.0%	0.03

Table 4: Fitting accuracies for Γ_h, B, and m_h of the SM Higgs with the 20-step scanning scheme with 3-MeV step size for three representative luminosities per step. Results with total integrated luminosity 0.5 fb^{-1} (1 fb^{-1}) for resolution $R = 0.01\%(0.003\%)$ are in boldface. This table is taken from Ref [8].

experimentalists. On the other hand, the beam profile is unlikely to be Breit-Wigner resonance profile. Thus an additional fitting parameter of the beam energy distribution is anticipated to provide us additional knowledge about the beam energy. Our estimated accuracies are by and large free from detector resolutions. Other uncertainties associated with b tagging, acceptance, etc., will enter into our estimation of signal strength B directly. These uncertainties will affect our estimation of total width Γ_h indirectly through statistics, leaving a minimal impact in most cases.

2.4 Potential to Resolve Nearly Degenerate Higgs Bosons

The scanning process not only provides high precision for the Higgs boson total width, but also high precision for the Higgs mass. Sub MeV level precision can be achieved as show in Table 4. This implies the muon collider to be an ideal machine to break the mass degeneracies between Higgs bosons. In this section, we discuss this potential of the muon collider.

There are many theoretical speculations about what we have observed at CERN LHC may be a combination of two nearly degenerate Higgs bosons [17, 18, 19, 20, 21, 22, 23]. This could happen in many models, for example, Two Higgs Doublet Models (2HDM) [17, 18, 19], 2HDM plus 1 Singlet Models, as well as Next-to-Minimal-Supersymmetric-Model [20, 21, 22]. We would like to point out that these speculations are all about GeV level degeneracy. It can be resolved easily at early stage of muon collider when determining the Higgs mass window, as described in Sec.2.2. In this section, we discuss about the MeV level achievable mass degeneracy resolution of the muon collider, which is also applicable to break the mass degeneracies in heavier Higgs bosons.

A naive expectation is that the muon collider could resolve the mass degeneracy to sub MeV level, as it does for the single Higgs boson mass fitting. However, this is way below the beam energy spread and the Higgs boson total width. The latter means the interference effect between these two highly degenerate Higgs bosons has to be taken into account at the muon collider. We demonstrate this resolution in Fig. 5 for $\mu^+\mu^- \to h, H \to b\bar{b}$. We fix the SM Higgs Boson at 126 GeV with total width 4.2 MeV. We set the other Higgs total width 10 MeV and the branching fractions to $b\bar{b}(\mu^+\mu^-)$ 90%(0.03%). This corresponds to a non-SM doublet Higgs with $tan\beta$ around 2 in Type II 2HDM, as well as (more likely) a larger $tan\beta$ with a significant mixing with additional singlet. We choose three difference masses from 126.01 GeV to 126.02 GeV and demonstrate both constructive interference and destructive interferences.

This mass degeneracy resolution depends on many factors, including the mass splitting, the total widths of both Higgs bosons, the relative sign of the amplitudes, the overall strength, the relative strength, and the beam energy resolution. The mass splitting and the total widths of both Higgs bosons determine the strength of the interference effect. The smaller the mass splitting comparing to the total widths, the stronger interference effects there will be. The relative sign of the amplitudes determines whether the interference to be constructive or destructive. The overall strength determines the how much statistics

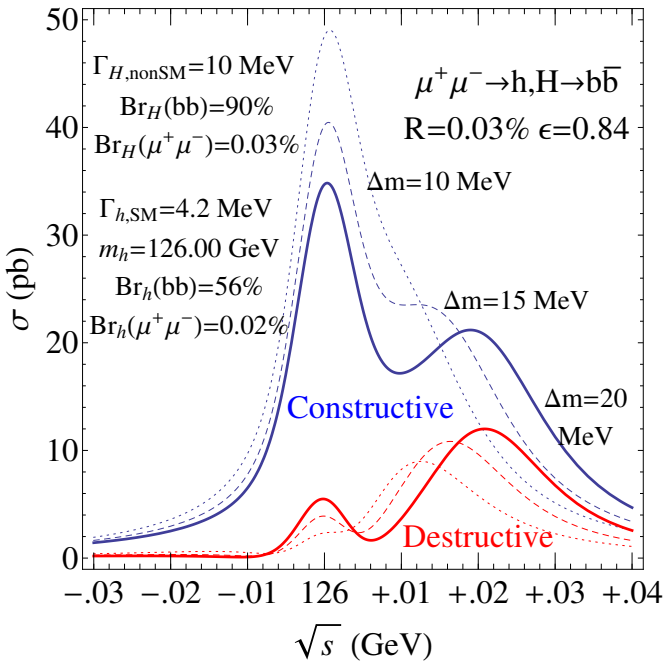

Figure 5: Resolving high degenerate Higgs bosons at the muon collider through scanning. The b-tagging efficiency is assumed to be 60 %, and the acceptance ϵ is thus 0.84 with at least one b-jet tagged. The solid, dashed and dotted lines represent mass splitting of the Higgs bosons 20 MeV, 15 MeV and 10 MeV. The blue and red curves represent constructive and destructive interferences, respectively.

we have at a given integrated luminosity. The relative strength affects the resolution in the sense that when one Higgs is dominate, the other insignificant one would be hard to separate at a fixed overall number of events. The optimal scenario would be both Higgs bosons having same total width and signal strength. Instead of this optimal scenario, our choice in Fig. 5 is more realistic with both Higgs bosons having same order of strength and total width. We can see the shape fitting is very necessary to resolute 10 MeV degeneracy. As a result, we argue the muon collider could resolve mass degeneracy to the level of these Higgs bosons' total widths.

There are other ways to resolve the mass degeneracy at the muon collider. For example, for 2HDM and related models, the other Higgs usually is expected not to couple to the vector bosons much. One could fit the mass from the WW^* mode to sub MeV level for the SM-like Higgs and fit the mass from $b\bar{b}$ mode to similar level. These two fittings shall have different best fitting masses and thus resolve the degeneracy. This scenario

Table 5: Sensitivity to the Standard Model Higgs Boson combining all modes. Low mass ≤ 130 GeV mode is principally $q\overline{q} \to (W, Z) + (h \to b\overline{b})$; higher mass ≥ 130 GeV mode is principally $q\overline{q} \to (W, Z) + (h \to WW^*)$.

Analyzable Lum/Expt	115 GeV	130 GeV	160 GeV
5 fb$^-$1	2.2 σ	1.7 σ	3.2 σ
10 fb$^-$1	3.1 σ	2.5 σ	4.6 σ
15 fb$^-$1	3.8 σ	3.0 σ	5.7 σ
20 fb$^-$1	4.4 σ	3.5 σ	6.5 σ

dependent method has the potential of resolving the mass degeneracy to MeV level.

To summarize, the muon collider Higgs factory is an ideal place to resolve the mass degeneracy of Higgs bosons. Its resolution should be the level of the Higgs bosons' total widths. This excellent mass degeneracy resolution can also be applied to the future upgrade of muon collider for energy frontier, where in many 2HDM and related models the heavier Higgs and CP-odd Higgs are highly degenerate.

2.4.1 $c\overline{c}$ (Purohit)

In the muon collider case, one expects 23,000 produced Higgs for an integrated luminosity of 1 fb^{-1}, which is effectively the number expected according to the ICFA report cited above. Once again, the branching fractions lead to approximately 800 $c\overline{c}$ decays and approximately 13,000 $h^0 \to b\overline{b}$ decays, implying a need to reject the $b\overline{b}$ background by a factor of 20 or more. Additionally, there is a long tail from Z decays which produces a background of 19 pb under the h^0 peak. [10] This tail therefore generates an additional 19,000 events.

Observing the h^0 peak should still be possible, but the background from Z-decays will be the dominant one after rejection of the $h^0 \to b\overline{b}$ decays. As shown in Fig. 6, excellent separation of charm and bottom jets is also possible for Higgs decays at the muon collider. A simple calculation of S/$\sqrt{B}$ implies an observation of the h^0 signal will be at the 5 to 6 sigma level.

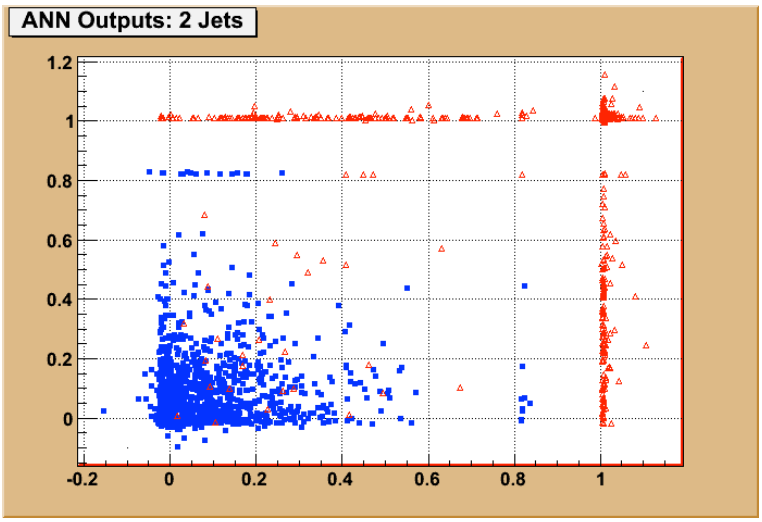

Figure 6: The two-jet ANN output plane for $\mu^+\mu^- \rightarrow h^0 \rightarrow 2$ heavy quark jets events in the detector. True c-jets are shown as blue squares, while the true b-jets are shown as red triangles.

3 Energy Determination by Spin Tracking

Raja and Tollestrup noted that the energy of the beams can be measured to high accuracy by tracking the precession of the decay electron energies. While stored, the muons continuously decay at $\cong 10^7$ decays per meter, and the electrons and positrons from the decay have a mean energy dependent on the polarization of the muons. That polarization, **P** will precess as the beam rotates around the ring and that precession will modulate the mean energy of decay electrons, and therefore the signal at a detector capturing those decays. In the present scenario the μ beams are created with a small polarization ($\approx$ 10 to 20%) from a bias toward capture of forward $\pi \rightarrow \mu$ decays) and that polarization should be substantially maintained through the cooling and acceleration systems. The mean energy from decay electrons is:

$$< E(t) >=< N \exp^{-\alpha t}(\frac{7}{20})E_\mu(1 + \frac{\beta}{7}P\cos(\omega t + \phi)) > \tag{3.3}$$

where N is the initial number of μs, E_μ is the μ energy, α is the decay parameter, $\beta = v/c$, P is the polarization, $\phi$is a phase, t is time in turn numbers and

$$\omega = 2\pi\lambda(\frac{g-2}{2}) \approx 2\pi \times 0.7 \tag{3.4}$$

is the precession frequency that depends on the muon beam energy. A detector capturing a significant number of decay electrons will have a signal modulated by that precession frequency, which can be measured to very high accuracy, obtaining an energy measurement to the 10^{-6} level (corresponding to 0.1 MeV), or better. A sequence of measurements will also obtain the width of the Higgs resonance to 0.1 MeV or better.

The precession observation gives the muon energy at each individual collision store. The precession signal decreases with time following the muon decay and the energy width, providing an important measurement of that width, which will assist in unfolding the Higgs width.

Raja and Tollestrup and Blondel analysed that property of a muon collider in 1998-2000. Blondel established that a polarization of 5% would be sufficient to enable this measurement. Simulations indicate that the muons should have an initial polarization of $\tilde{1}$0-20 % and that polarization would be maintained in cooling and acceleration. More detailed modeling at the currently known Higgs mass and collider and detector parameters are needed to verify the potential measurement accuracies.

4 Accelerator Backgrounds

The potential to perform physics with a muon collider will largely be determined by how well one can suppress the accelerator backgrounds from the collider ring. The source of most of the accelerator backgrounds in a muon collider is associated with the decay of beam muons. Studies to date have utilized backgrounds generated for a 1.5 TeV collider. Specific backgrounds for a 126 GeV Higgs Factory are not yet available. Both the 1.5 TeV machine and Higgs factory designs assume 2 x 10^{12} muons per bunch which will produce 4.3×10^5 or 6×10^6muon decays per meter for the 1.5 TeV and 126 GeV machines.

The electrons resulting from muon decays will interact with the walls of the beam chamber, collimators, and shielding, producing high energy electromagnetic showers, synchrotron radiation, photo nuclear interactions, and Bethe-Heitler muons. Photonuclear interactions with the nuclei of beam pipe, magnet or shielding material from energetic photons in the electromagnetic shower are the main source of the hadronic and neutron background. Neutrons are predominantly produced from photonuclear spallation processes in the giant resonance region (14-20 MeV incident gammas).

A preliminary study of backgrounds in a 1.5TeV (750 GeV on 750 GeV) muon collider was done utilizing GEANT4 (through G4Beamline [41]) and MARS. The goal of the

study was to calculate the accelerator-generated backgrounds that could arrive at a muon collider detector. The lattice design for this machine is described in Ref. [42], with a description of the interaction region design given in Ref. [43]. In this study the lattice was modelled at ±75 m from the interaction point. Electrons from muon decays are assumed to originate at locations uniformly distributed along the μ^+ and μ^- reference trajectories.

Figure 7 shows the background flux entering the detector region in a typical Muon Collider interaction. Total non-ionizing background is about 10% that of the LHC, but the crossing interval is 400 times longer, resulting in high instantaneous flux. The background is very different in character than that of either the LHC or CLIC. It is dominated by soft photons and low energy neutrons emerging from the shielding surrounding the detector. A typical background event has 164 TeV of photons, 172 TeV of neutrons, and 184 TeV of muons. With the exception of muons and charged hadrons the background spectrum is dominated by low energy particles. Only a small fraction of the background originates from the vicinity of the interaction region. This means that most of the decay background is out of time with respect to particles originating from the $\mu^+\mu^-$ collision.

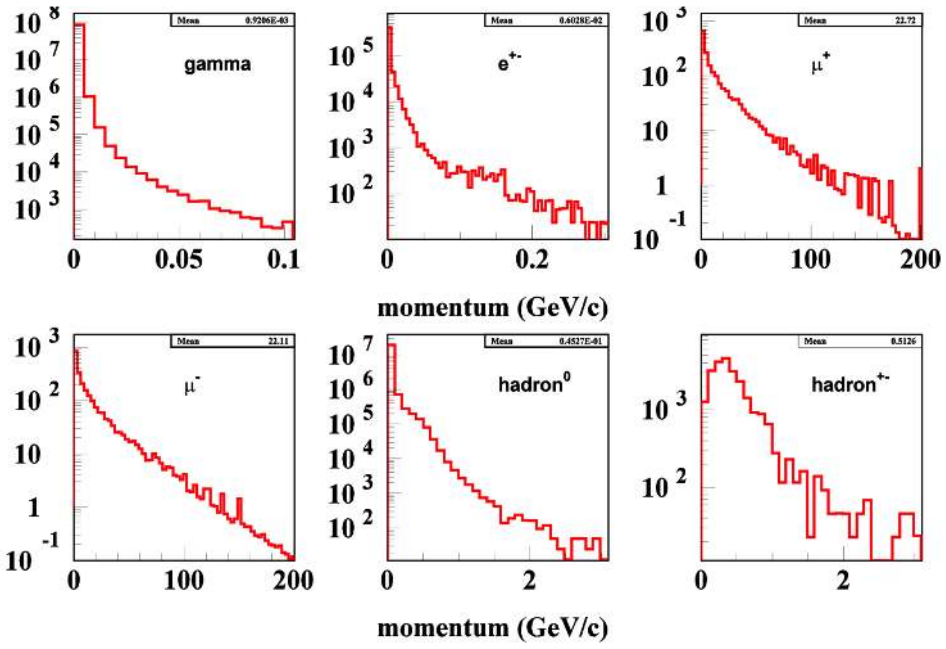

Figure 7: Energy distributions of particles entering the detector region from a MARS simulation of Muon Collider beam backgrounds[?].

5 Background Rejection Techniques

Extensive studies [47] for 0.75x0.75 TeV Muon Collider resulted in a design of the collider lattice, magnets show that with a detector shielding nozzle with cone angle of 10° the total number of the background particles entering the detector can be reduced by three orders of magnitude. Simulation of the background was done with the MARS15 code [48]. According to [47] the remaining detector background particles are mainly low energy photons and neutrons ($\sim$1.8x10^8 and $\sim$0.4x10^8 particles per crossing respectively). The e^+ and e^-, charged hadrons and muons comprise less than 0.5% of the background ($\sim$1x10^6, $\sim$5x10^4 and $\sim$0.8x10^4 particles respectively).

The fact that much of the background is soft and out of time gives us two handles on the design of an experiment that can cope with the high levels of background. Timing is especially powerful. The local gate t=0 is defined as the time when relativistic particle emerging from the interaction point arrives at the detector. Therefore a very tight cut can be made, still preserving the bulk of the tracks of interest. A 3 ns cut rejects two orders of magnitude of the overall background and about 4 orders of magnitude of neutron background.

A study of timing for hits produced in vertex (VXD) and tracker silicon detectors by 0.75x0.75 TeV Muon Collider background particles and IP muons was done recently and reported in [50]. The ILCroot simulation framework [51] was utilized. The layout of the VXD and Tracker is based on an evolution of SiD and SiLC trackers in ILC (see detail in [49]). In the analysis the time of flight (TOF) of hits given relative to the bunch crossing time was recalculated relative to T0 - time of flight for a photon from interaction point (IP) (x=0,y=0,z=0) to the detector plane. Detector electronics would likely digitize and time stamp hits within a larger ($\approx 10ns$) window to allow for fitting of slow heavy particles using time of flight as a fitting parameter. The implementation of such time cuts can reduce the occupancy of the readout hits in VXD and Tracker layers to the level acceptable for efficient tracking of physics tracks as was shown in [49].

Figure 8 shows IP muon hit inefficiency and fraction of hits from background particles versus the timing gate width at 0.5 ns hit resolution time. As we can see, a timing gate width of 4 ns can provide a factor of 300-500 background rejection keeping efficiency of hits from IP muons higher than 99%.

Timing is also crucial for background rejection in the calorimeter. A calorimeter design studied by R. Raja [**?**]. combines fast timing with the reconstruction ability of pixelated

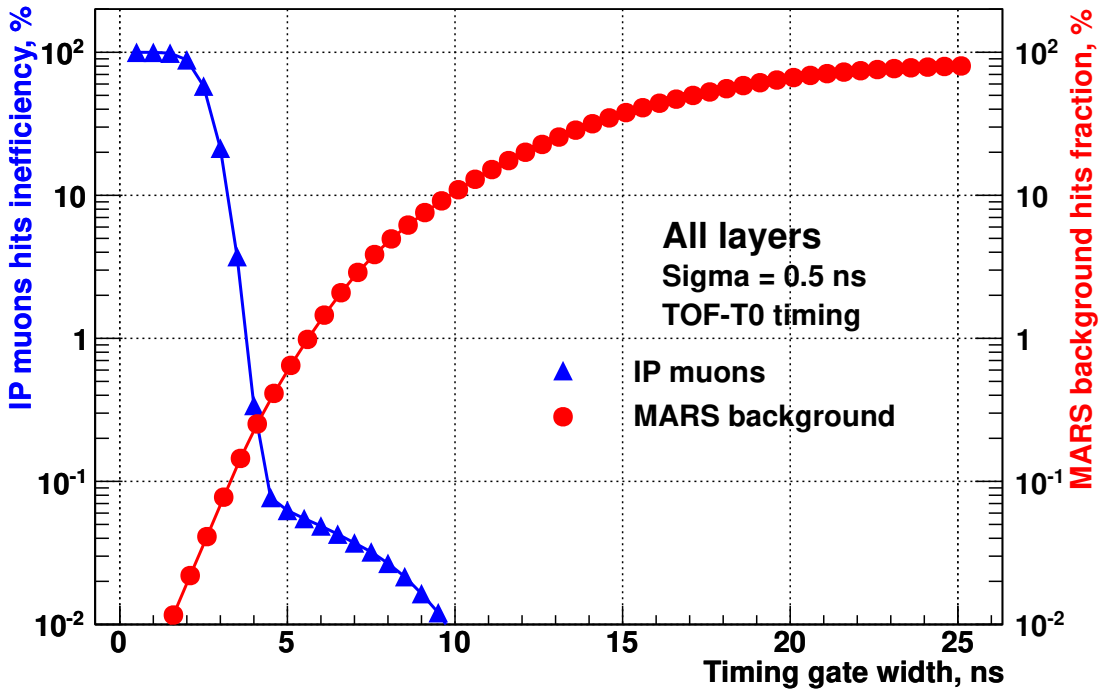

Figure 8: Inefficiency of IP muon hits and fraction of MARS background particles hits in the VXD and Tracker Si detectors versus width of timing gate at the hit time resolution σ=0.5 ns.

calorimeters being studied for particle flow. In this design a pixelated imaging sampling calorimeter with 200 μm square cells and a 2 ns "traveling trigger" gate referenced to the time of flight with respect to the beam crossing is used to reject out-of-time hits. This sort of calorimeter can also implement compensation by recognizing hadronic interaction vertices and using the number of such vertices to correct the energy. Initial estimates of the resolution of such a compensated calorimeter is $60\%/\sqrt{E}$. In contrast to relativistic tracks and electromagnetic showers, hadronic showers can take significant time to develop[**?**]. Initial studies of a dual readout total absorption calorimeter for the Muon Collider also show that resolution lost to a fast time gate can be regained by utilizing a dual readout correction. A summary of the tracking and pixelated calorimetry background rejection factors for a 1.5 TeV collider are shown in table 5.

We have learned that tracking is feasible in a Muon Collider detector. Calorimetery is more challenging, but progress is being made on calorimeter concepts that appear to meet the physics needs. The large background of non-ionizing radiation means that silicon

Calorimeter background Energy				Tracker Background hits	
Type	Energy before cuts (TeV)	Energy after 2ns cut (GeV)	Rejection (2 ns cut)	Radius (cm)	Rejection (1 ns cut)
EM	170	404	2.4×10^{-3}	20	1.2×10^{-3}
Muons	185	47	0.25×10^{-3}	46	0.8×10^{-3}
Mesons	7	51	7.5×10^{-3}	72	1.1×10^{-3}
Baryons	178	386	2.1×10^{-3}	97	0.6×10^{-3}

Table 6: Rejection of beam background calorimeter energy and tracker hits for a 1TeV Muon Collider with timing windows with respect to time of flight from the primary vertex of 2 and 1 ns respectively.

tracker will have to be kept cold, around -10 C, increasing the detector mass. Precise timing and pixelated detectors will be crucial to a successful Muon Collider detector. Both come at a cost. Fast electronics will necessarily dissipate significant power and, in contrast to planned ILC detectors, detectors for the Muon Collider will have to be liquid (CO_2) cooled with an associated increase in mass with respect to ILC trackers.

6 Detector Design

The next generation of collider detectors will emphasize precision for all sub-detector systems. In the case of a muon collider Higgs factory the $h \to b\bar{b}$ and $h \to \tau^+\tau^-$ channels require good b-tagging and vertexing capabilities. The $h \to WW^*$ channel will require the capability to distinguish W and Z vector bosons in their hadronic decay mode while $h \to \gamma\gamma$ emphasizes excellent energy and position measurement of photons[1] . To achieve the tracking goals we require a high solenoidal magnetic field of 5 Tesla and high precision low mass tracking. To achieve good jet resolution the electromagnetic and hadronic calorimeter have to be located within the solenoid. The machine induced background from μ decays upstream and down stream of the interaction point provide a very challenging environment but this background is out of time compared to the particles from the interaction point. Therefore for both tracker and calorimeter good timing resolution (in order of nsec) will be crucial to reduce this background to an acceptable level. This backgrounds make shielding necessary extending into the tracker volume. Figure 9 shows an Illustration of the detector as it is currently implemented in the Geant 4 simulation. The tungsten shielding cone is well visible. Here we present an idealistic conceptual design that will have to be replaced by an optimized, more realistic and cost efficient design in the future.

6.1 Tracking

To achieve the tracking goals while keeping the tracker compact we require a high solenoidal magnetic field of 5 Tesla and use silicon tracking paired with a pixel vertex detector for high precision low mass tracking. Fast timing and fast readout requires extra power and cooling and R&D will be necessary to achieve this while keeping detectors and support at the required low mass. Figure 10 shows the layout of the tracking and vertex detector. The vertex barrel detector is assumed to consist of 5 barrel layers with $20\mu m$ square pixels and 0.8% radiation length per layer, the six vertex disks are assumed to utilize $50\mu m$ square pixels with 1.0% radiation length. The four tracker barrel layers and four disk layers are assumed to have $100 \times 1000\mu m$ short strips with 1.5% radiation length per layer.

[1]The discovery of the Higgs in the $h \to \gamma\gamma$ channel at the LHC provides a strong argument requiring good energy resolution for photons.

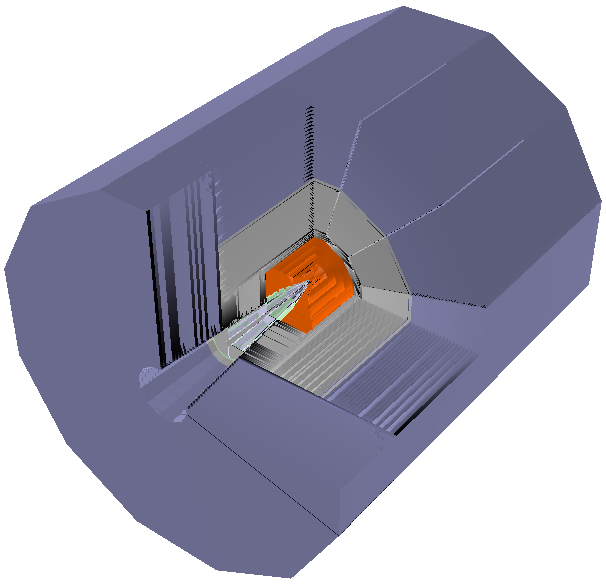

Figure 9: Illustration of the mcdrcal01 detector.

6.2 Calorimetry

A common benchmark for ILC detectors is to distinguish W and Z vector bosons in their hadronic decay mode. This requires a di-jet mass resolution better than the natural width of these bosons and hence a jet energy resolution better than 3%. For hadron calorimetry this implies an energy resolution a factor of at least two better than previously achieved to date by any large-scale experiment. A novel approach to achieving superior hadronic energy resolution is based on a homogeneous hadronic calorimetry (HHCAL) detector concept, including both electromagnetic and hadronic parts, with separate readout of the Cerenkov and Scintillation light and using their correlation to obtain superior hadronic energy resolution [29], [30]. This HHCAL detector concept has a total absorption nature, so its energy resolution is not limited by the sampling fluctuations. It has no structural boundary between the ECAL and HCAL, so it does not suffer from the effects of dead material in the middle of hadronic showers in addition there is no difference in response since ECAL and HCAL are identical and only the segmentation differs. It also takes advantage of the dual readout approach by measuring both Cerenkov and scintillation light to correct for the fluctuations caused by the nuclear binding energy loss, so a good energy resolution for the hadronic jets can be achieved [31], [29],[30]. To improve event recon-

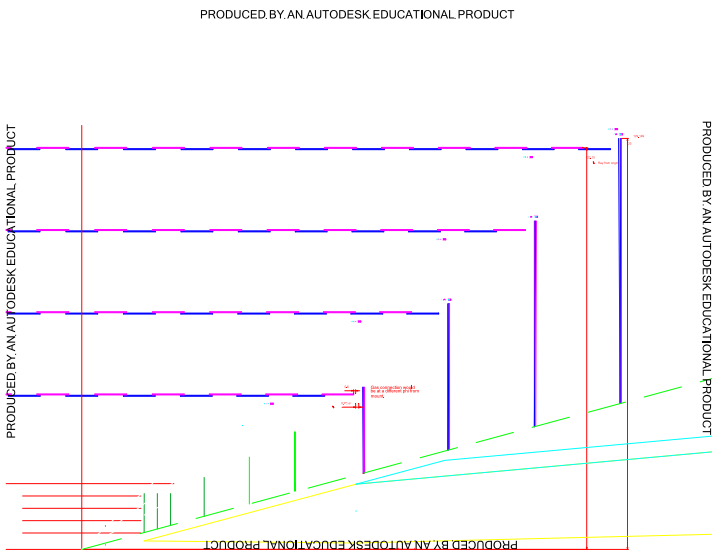

Figure 10: Layout of the vertex and tracking detector barrel and endcaps and the tungsten shielding cone.

struction we plan to use particle flow algorithms therefore we require fine segmentation (granularity) of the calorimeter. A cost effective active material is crucial for the HHCAL detector concept and R&D is necessary to find the appropriate active materials, such as scintillating crystals, glasses or ceramics to be used to construct an HHCAL. With regards to photosensors silicon-based photo detectors (a.k.a SiPM, MPPC) are reaching a very mature state and are becoming potential photo-transducers for hadron calorimetry for selectively detecting scintillation and Cerenkov light. The parameters and segmentation of the mcdrcal01 calorimeter are listed in Table 7.

6.3 The software environment

We used and extended the ALCPG[2][33] software suite. Using this software suite enables us to utilize existing standard reconstruction software modules for Digitization, cluster algorithms, hit manipulation, tracking etc. that are part of the software package.

The ALCPG software suite consists of:

- SLIC[3], to simulate the detector response. SLIC is a full simulation package that uses

[2]American Linear Collider Physics Group
[3]Simulator for the Linear Collider

	electromagnetic (em)	hadronic (had)	muon
Material	BGO/PbF_2		$Iron$
density $[g/cm^3]$	7.13/7.77		7.85
radiation length $[cm]$	1.1/0.93		1.76
nuclear interaction length (IA) $[cm]$	22.7/22.4		16.8
Number of layers	10	30	22
Thickness of layers $[cm]$	2	5	10
Segmentation $[cm \times cm]$	1×1	2×2	10
total depths $[cm]$	20	150	220
total IA	em + had: 7.5/7.6		13.1

Table 7: Properties of calorimeter and instrumented Iron flux return for Barrel and Endcaps.

the Geant4 Monte Carlo toolkit [36] to simulate the passage of particles through the detector. The SLIC software package uses LCDD[4][35] for its geometry input. LCDD itself is an extension of GDML[5] [40]. LCDD makes it easy to quickly implement new detector detector concepts which is especially useful in the early stages of developing and optimizing a detector concept

- lcsim.org [38], is a reconstruction and analysis package for simulation studies for the international linear collider. It is entirely developed in Java for ease of development and cross-platform portability.

- JAS3[6][37] is a general purpose, open-source data analysis framework. The following features are provided in form of plug ins:

  - LCIO Event Browser.
  - WIRED 4[39] is an extensible experiment independent event display.
  - AIDA[7] compliant analysis system. It provides tools for plotting of 1d, 2d and 3d histograms, XY plots, scatterplots etc. and fitting (binned or unbinned) using an extensible set of optimizers including Minuit.

[4]Linear Collider Detector Description
[5]Geometry Description Markup Language
[6]Java Analysis Studio
[7]Abstract Interfaces for Data Analysis

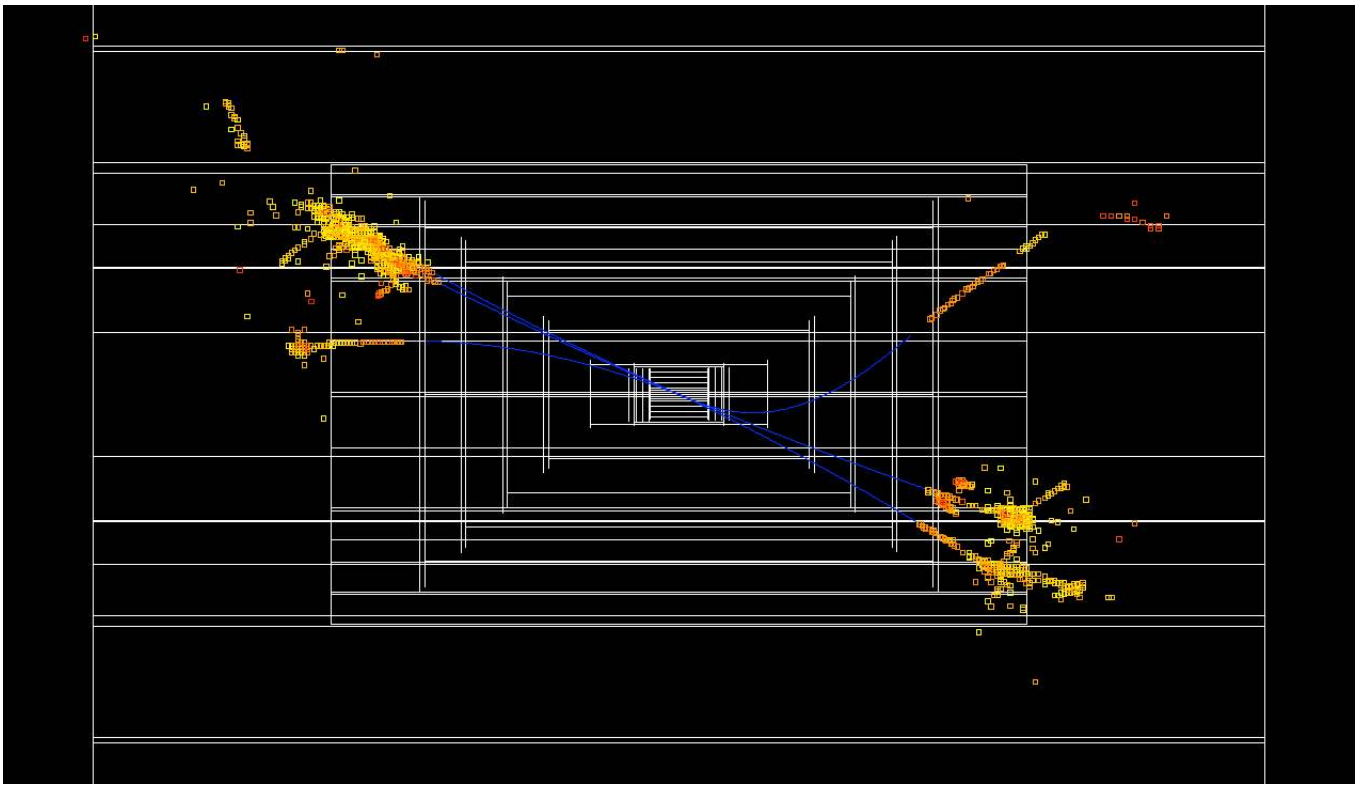

Figure 11: Wired display of a $h \to \tau^+\tau^-$ event in the mcdrcal01 detector.

7 Studies of Higgs Physics (Conway and Wenzel)

In light of the recent discovery of an approximately 126 GeV Higgs boson at the LHC, the particle physics community is beginning to explore the possibilities for a next-generation Higgs factory particle accelerator. In this report we study the s-channel resonant Higgs boson production and Standard Model backgrounds at a proposed $\mu^+\mu^-$ collider Higgs factory operating at center-of-mass energy $\sqrt{s} = M_H$ with a beam width of 4.2 MeV. We study PYTHIA-generated Standard Model Higgs and background events at the generator level to identify and evaluate important channels for discovery and measurement of the Higgs mass, width, and branching ratios. We find that the $H^0 \to b\bar{b}$ and $H^0 \to WW^*$ channels are the most useful for locating the Higgs peak. With an integrated luminosity of 1 fb^{-1} we can measure a 126 GeV Standard Model Higgs mass accurately to within 0.25 MeV and its total width to within 0.45 MeV. Our results demonstrate the value of the high Higgs cross section and narrow beam resolution potentially achievable at a muon collider.

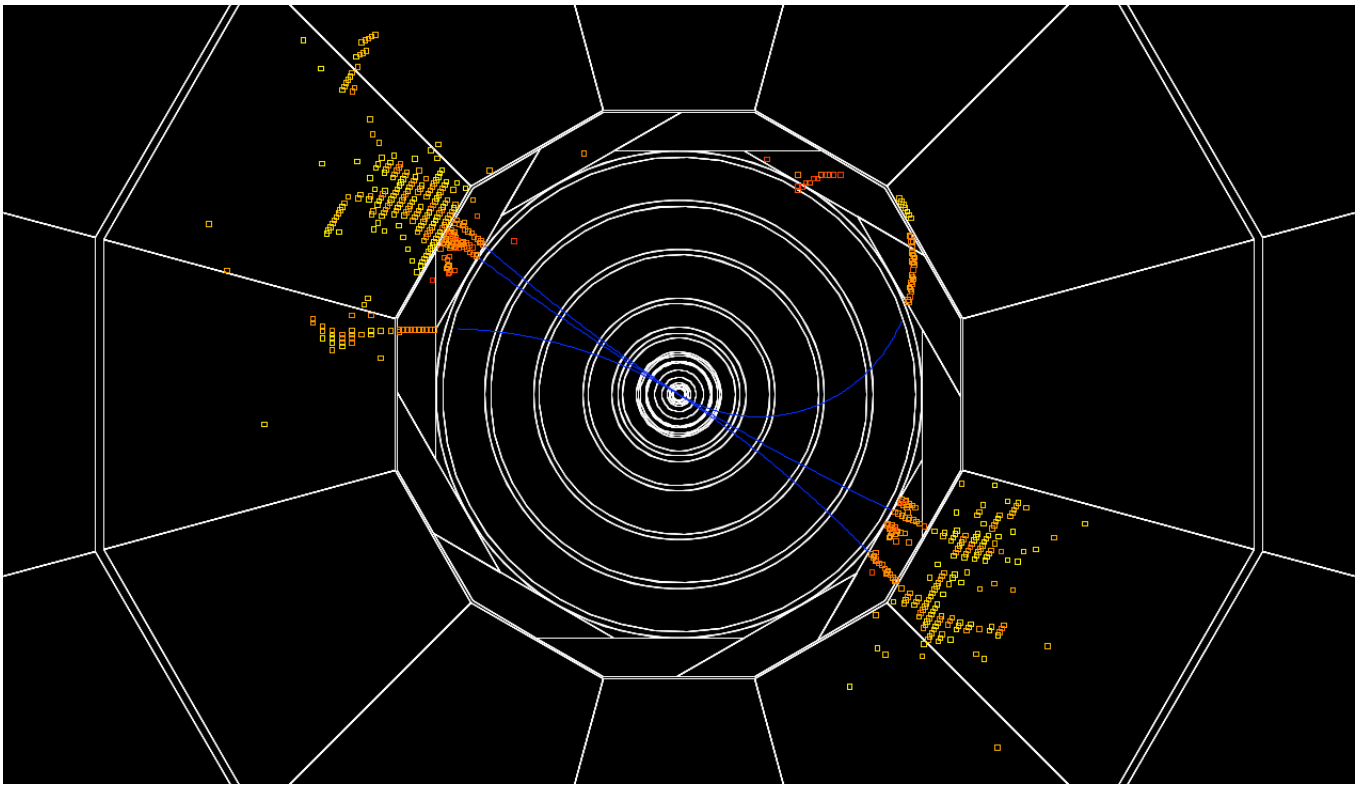

Figure 12: Wired display of a $h \to \tau^+\tau^-$ event in the mcdrcal01 detector.

7.1 Physics Background

The most significant background for s-channel resonance Higgs production at a muon collider is the production of Z bosons. The Higgs cross section, smeared by a 4.2 MeV beam is 28.3 pb. The cross section of the Z background is 376 pb, but 20.04% of these Z's decay into pairs of neutrinos and a photon, bringing the cross section to 301.4 pb and $S/\sqrt{B}$ to 1.63. This cross section remains essentially flat in the region around the Higgs peak and will be treated as such in this report. Figure 13 shows simulated data of a scan across a 126.0 GeV Higgs peak counting all events except for $Z^0 \to \nu_\ell \overline{\nu_\ell}$. The data is fitted to a Breit-Wigner convoluted with a Gaussian with three free parameters; Γ_H, M_H and $Br(H^0 \to X)$. The fixed parameters are the background cross section $\sigma(Z^0 \to X)$, the beam width σ_{beam} and the total integrated luminosity $\mathcal{L}$. The fit gives a width of 4.56 ± 1.52 MeV, an error in the mass measurement of 0.13 ± 0.16 MeV and a branching ratio of 0.96 ± 0.04.

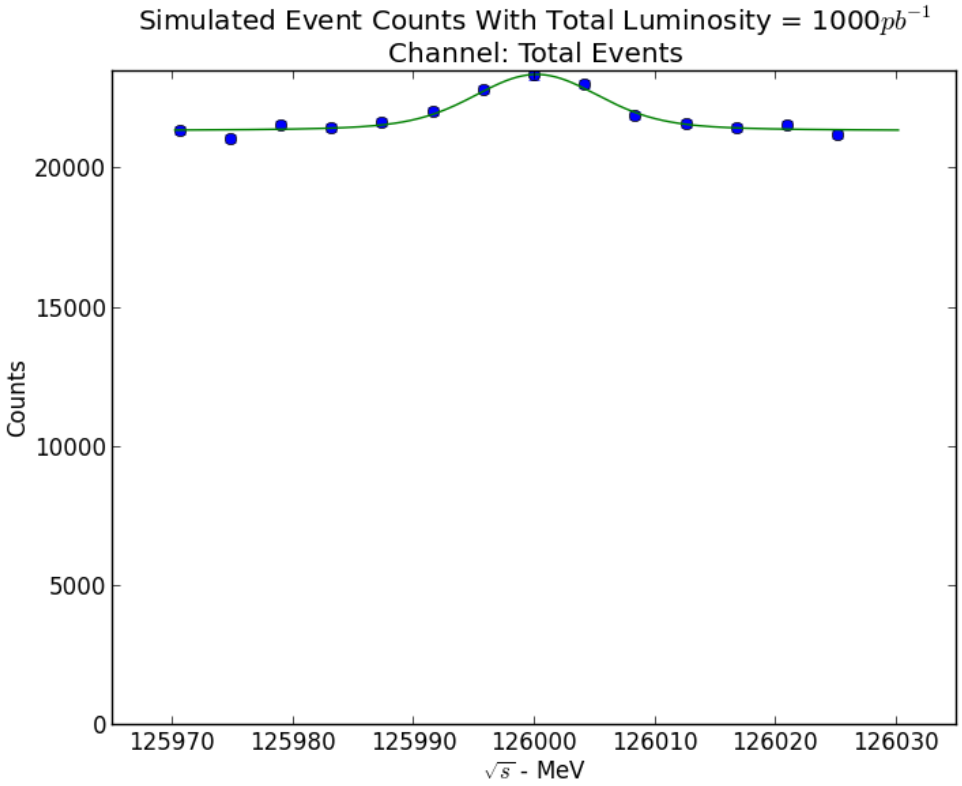

Figure 13: Simulated event counts for a scan across a 126.0 GeV Higgs peak with a 4.2 MeV wide Gaussian beam spread, counting all events except for $Z^0 \to \nu_\ell \overline{\nu_\ell}$ decays. Data is taken in a 60 MeV range centered on the Higgs mass in bins separated by the beam width of 4.2 MeV. Total luminosity is 1 fb^{-1}. Event counts are calculated as Poisson-distributed random variables and the data is fit to a Breit-Wigner convoluted with a Gaussian peak plus linear background. Fitted values of the free parameters are in Table 9.

7.2 Low-Mass Z bosons

Fortunately, this background is reducible. The s-channel resonance production of Higgs bosons only happens with a center of mass energy within a few MeV of its peak. Z bosons however are produced in several different processes with a wide range of masses, as seen in Figure 14. At an s-channel Higgs factory muon collider, Z bosons are primarily produced as real, on-shell bosons along with an intial state photon that makes up the difference in energy between the Higgs s-channel and the Z mass (Fig. 15(b)). There is also a small number of very low mass Z bosons produced in a Drell-Yan process. The only events that are theoretically indistinguishable from Higgs events are those where a virtual Z is produced at the center of mass energy and decays into a channel shared with the Higgs

(Fig. 15(a)).

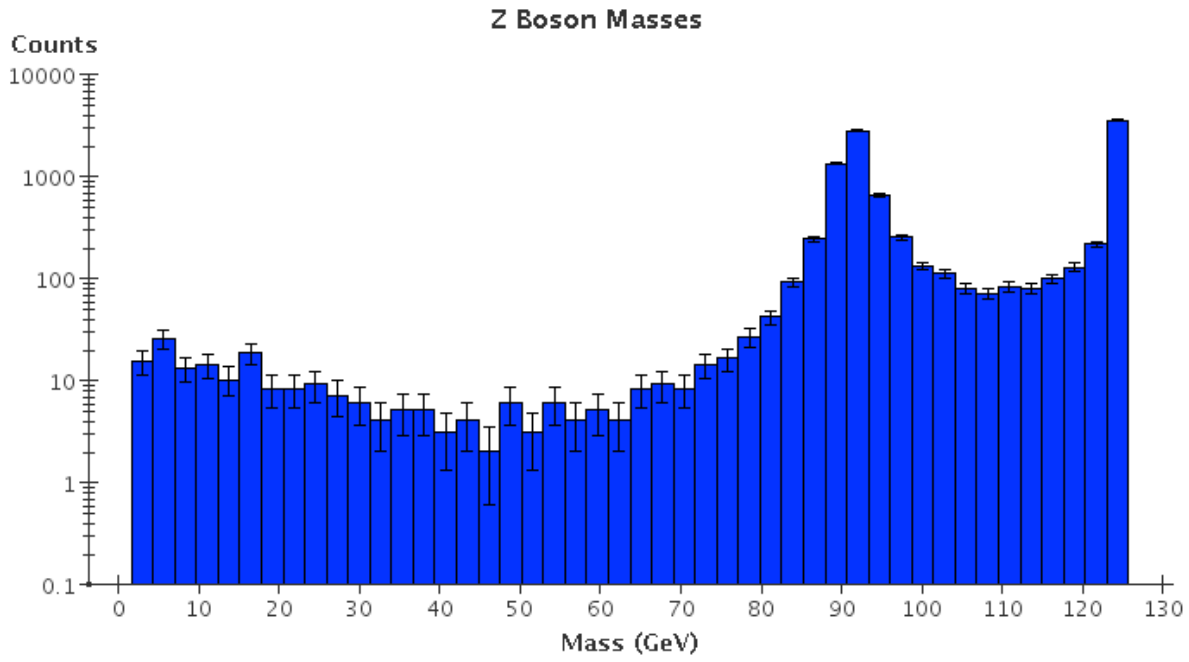

Figure 14: Z boson masses in 10,000 PYTHIA-simulated $\mu^+\mu^- \rightarrow Z$ events at $\sqrt{s} = 125.0GeV$. The low-mass region is dominated by the Drell-Yan process. There is a peak around the Z mass where intial-state Bremsstrahlung radiation allows the creation of an on-shell Z. The third region of interest is the peak at $125GeV$, the center of mass energy. This represents a process with no initial state radiation where the off-shell Z's produced are indistinguishable from the Higgs.

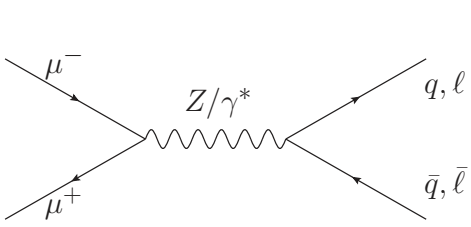

(a) Irreducible background: $\mu^+\mu^- \rightarrow Z/\gamma^*$ with $M_{Z^*} = \sqrt{s}$.

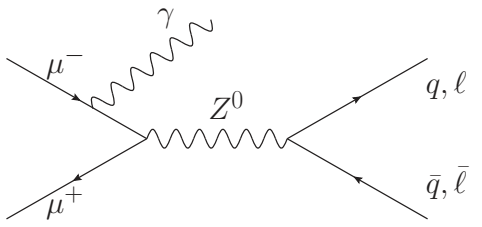

(b) Reducible background: $\mu^+\mu^- \rightarrow Z^0, \gamma$ with $M_{Z^0} < M_{H^0}$.

Figure 15: Standard Model backgrounds at a $\mu^+\mu^-$ collider operating at $\sqrt{s} = 126\ GeV$

Before looking into how the kinematics of these events might differ from Higgs events, the simple thing to do is a cut on the total energy potentially visible to the detector. This is accomplished by summing the energies of all final state particles which pass a

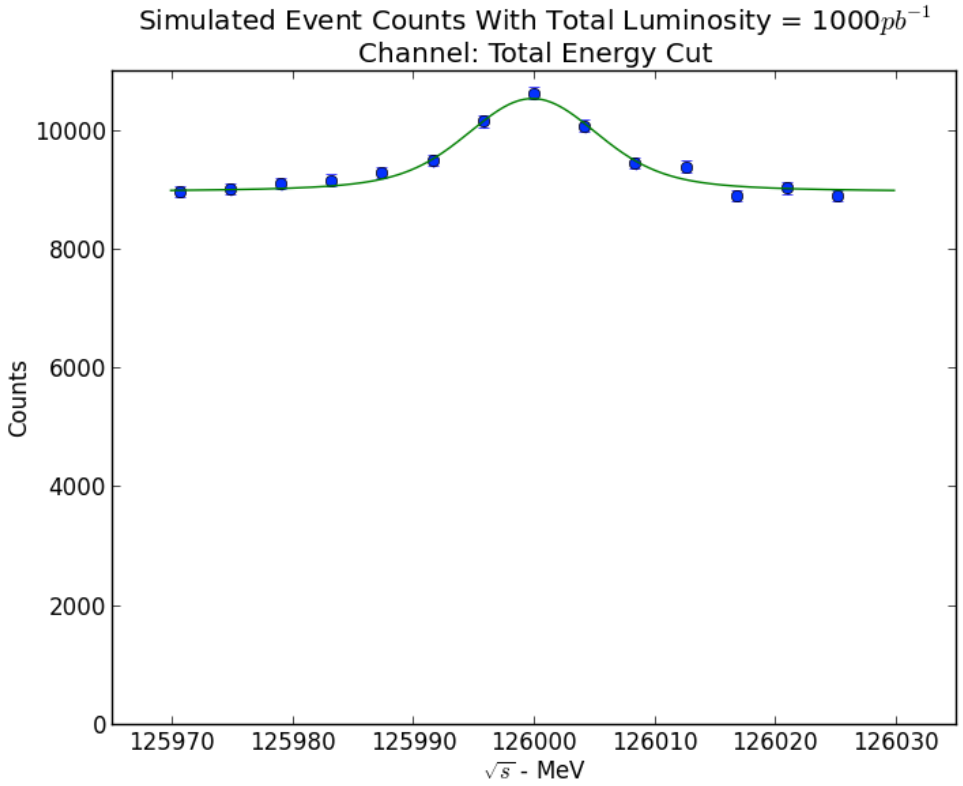

Figure 16: Simulated event counts for a scan across a 126.0 GeV Higgs peak with a 4.2 MeV wide Gaussian beam spread, counting all events with a total energy of at least 98.0 GeV visible to the detector. Data is taken in a 60 MeV range centered on the Higgs mass in bins separated by the beam width of 4.2 MeV. Event counts are calculated as Poisson-distributed random variables and the data is fit to a Gaussian peak plus linear background. The fit width is 5.16 ± 0.24 MeV and the error in the mass measurement is 0.26 ± 0.19 MeV.

$\cos\theta < 0.94$ cut and finding the energy cut which maximizes $S/\sqrt{B}$. The $\cos\theta$ cut is effective because most of the high-energy initial state radiation is colinear with the beam. We use a cut of $E_{total} > 98.0\ GeV$, which selects 79.2% of the Higgs signal events and 41.9% of the Z background. This results in an effective Higgs cross section of 22.4 pb and a background of 126.4 pb, bringing $S/\sqrt{B}$ to 1.99. Figure 16 shows simulated data using these results, with a fitted width of 5.57 ± 1.33 MeV and an error in the mass measurement of -0.02 ± 0.14 MeV. This simple cut has already proven to be a marginal improvement but there is much more that can be done by focusing on individual decay channels.

Decay Mode	Z		H^0	
	BR	σ (pb)	BR	σ (pb)
$u\bar{u}$,$d\bar{d}$,$s\bar{s}$	0.427	160.6	0.0003	0.009
$c\bar{c}$	0.119	44.8	0.032	0.91
$b\bar{b}$	0.152	57.2	0.584	16.5
e^+e^-	0.034	12.8	—	—
$\mu^+\mu^-$	0.034	12.8	—	—
$\tau^+\tau^-$	0.034	12.8	0.071	2.01
$\nu_\ell\overline{\nu_\ell}$	0.200	75.4	—	—
gg	—	—	0.053	1.50
$\gamma\gamma$	—	—	0.003	0.085
WW^*	—	—	0.226	6.39
Z^0Z^0	—	—	0.028	0.79
Total:	1.0	376.3	1.0	28.3

Table 8: Branching fractions and effective cross sections for Standard Model decay modes of Higgs and Z bosons. Higgs cross sections are calculated as the peak value of the Higgs peak Breit-Wigner convoluted with a Gaussian of width 4.2 MeV to simulate the effect of beam smearing. Branching fractions are taken from PYTHIA 6.4 event generation output.

7.2.1 $b\bar{b}$

Table 8 compares the branching ratios and cross sections of the Z background with the Higgs signal. The largest Higgs decay channel is $H^0 \to b\bar{b}$, which makes up 58% of Higgs decays at this mass, a branching fraction proportionally large to $Br(Z^0 \to b\bar{b}) = 15.2\%$. We assume a b-tagging efficiency and purity of 1, so the cross sections for the decays are 16.5 and 57.2 pb, respectively. The fitted values for the mass, width and branching ratio of the Higgs using b-tagging are shown in Table 9 and a fit to simulated data can be found in Appendix **??**.

In both signal and background the visible energy spectrum is very similar to the spectrum of the combined channels, so the same total energy cut of $E_{tot} > 98.0GeV$ maximizes $S/\sqrt{B}$. Cuts on the event shape, the magnitude of the thrust and major axis, can further enhance the signal. The event shape is calculated by finding the axis which maximizes the sum of all particle momenta projected onto a single axis, called the 'thrust axis'. This is then repeated for an axis perpendicular to the first and then a third orthogonal to both. The thrust is the normalized sum of the projection of all particle momenta against the thrust axis and the major axis value is the normalized sum of the

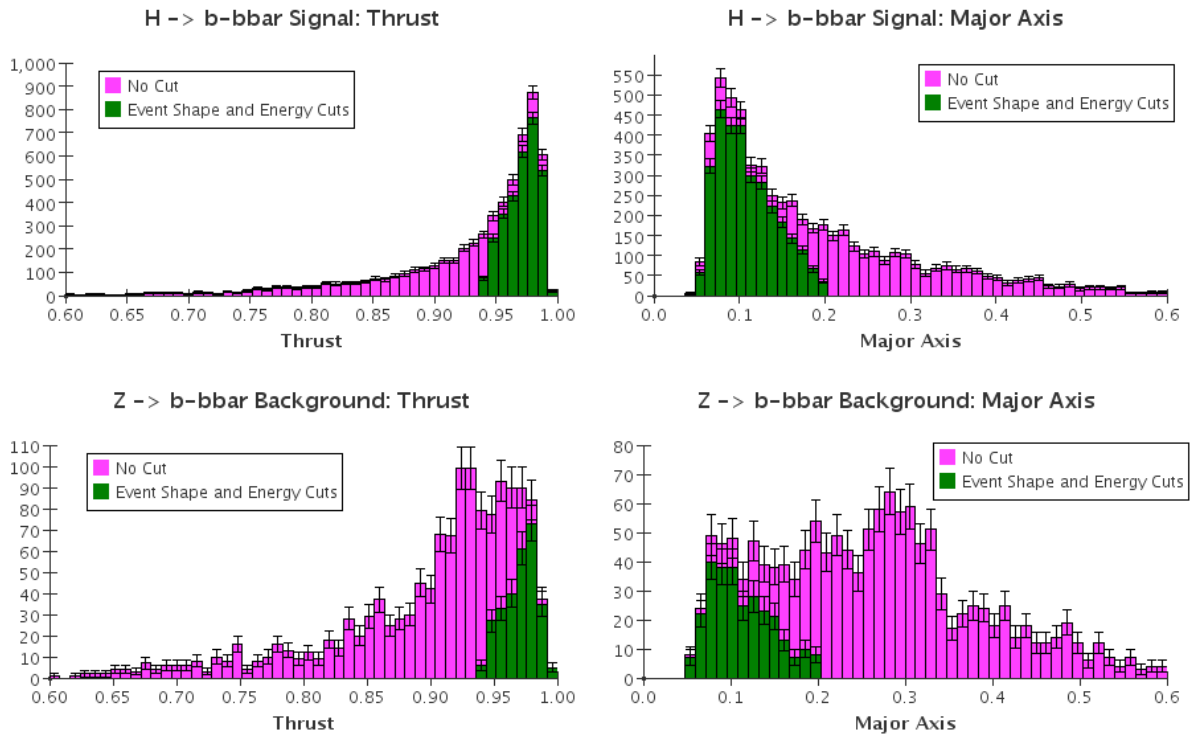

Figure 17: Effects of event shape and energy cuts on Higgs $b\bar{b}$ signal and background. Cuts were made by selecting events with total energy $E_{tot} > 98.0GeV$ visible to the detector, thrust between 0.94 and 1.0 and major axis between 0.0 and 0.2. The signal is reduced to 52% and the background to 15%.

projections against the secondary axis. Because the Higgs is never created in events with significant beamstrahlung it is always produced with low momentum. Z bosons produced with mass lower than the beam center-of-mass energy are 'boosted' by the beamstrahlung photon. This boost lowers the thrust and raises the major axis values, so it is a useful indicator for channels with particular event shape profiles.

Figure 17 shows the signal and background thrust and major axes before and after cutting on the total energy and event shape values. The cuts were made by selecting events with $E_{tot} > 98.0GeV$, thrust values between 0.94 and 1.0 and major axis values between 0.0 and 0.20. We continue to assume perfect b-tagging. These cuts reduce the $b\bar{b}$ signal by 52% and the background by 15%, bringing the effective cross sections to 8.64 and 8.45 pb respectively. This brings the $S/\sqrt{B}$ ratio to 2.97, a dramatic improvement over simple energy cuts or b-tagging alone. Figure 18 shows a simulated scan of the Higgs peak with a fit to a Breit-Wigner convoluted with a Gaussian.

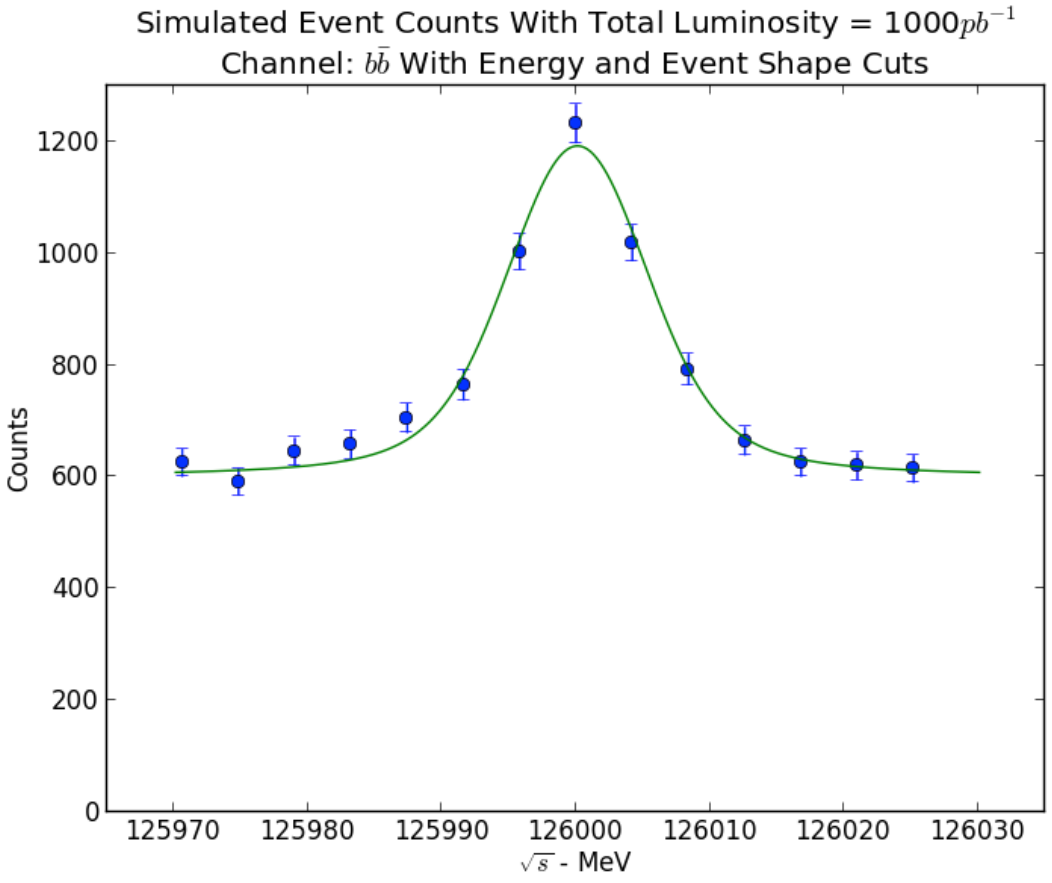

Figure 18: Simulated event counts for a scan across a 126.0 GeV Higgs peak with a 4.2 MeV wide Gaussian beam spread, counting $X \to b\bar{b}$ events with a total energy of at least 98.0 GeV visible to the detector and cutting on event shape parameters. Data is taken in a 60 MeV range centered on the Higgs mass in bins separated by the beam width of 4.2 MeV. Event counts are calculated as Poisson-distributed random variables and the data is fit to a Breit-Wigner convoluted with a Gaussian plus linear background. The fit width is 4.78 ± 0.48 MeV, the error in the mass measurement is 0.01 ± 0.05 MeV and the branching ratio is measured at 0.271 ± 0.001. Total luminosity is $1000pb^{-1}$, or $71.4pb^{-1}$ per point.

7.2.2 $H^0 \to WW^*$

There are several channels with very little physics background that are of importance, despite their smaller cross sections. One of these is the $H^0 \to WW^*$ decay mode, with a branching fraction of 0.226 (cross section 6.39 pb) and no real background from the corresponding Z decays. The W boson decays into a charged lepton and corresponding neutrino 32.4% of the time, with effectively equal rates for each type of lepton. The majority of the remaining branching fraction is the decay into pairs of light quarks. While it is certainly possible to reconstruct W bosons from four-jet events, in this report we focus on the decays with missing energy in the form of neutrinos since they can be identified by the presence of one or two isolated leptons and missing energy and are the most common. Further study will be required for a detailed analysis of the four-jet case. Since the W boson decays into a lepton and neutrino 32.4% of the time and we require at least one such decay between a pair of W's, these make up 54.3% of WW^* events. Thus the theoretical cross section is 6.39 pb with virtually no background.

Because the detector will have a non-sensitive cone, there will be a small amount of 'fake' background, eg. when the photon in the decay $\mu^+\mu^- \to Z^0 + \gamma \to \ell^+ + \ell^-$ boosts the two leptons and disappears into the cone as missing energy. Figure **??** in Appendix **??** shows an example event display for a WW^* decay into two leptons and illustrates the characteristic missing energy of these events. It is difficult to estimate the true background from processes such as these, but given the low branching ratios of Z^0 to lepton pairs and the kinematic and geometric constraints for 'fake' background, it is safe to assume that the background will be fairly low in this channel. Therefore we use the rate assumed by Han *et al*[**?**], a cross-section of 0.051 pb. Plots of simulated data for the WW^* channel can be found in Appendix **??** and fitted values in Table 10.

7.2.3 $\tau^+\tau^-$

The $\tau^+\tau^-$ channel is dominated by the background, but the Higgs branching ratio of 0.071 is not insignificant. The $Z^0 \to \tau^+\tau^-$ process has a branching ratio of 0.034, giving it an effective cross section of 12.8 pb, compared to the 2.01 pb cross section for the Higgs. However, the boost given to the lower mass Z bosons means the background can be further distinguished using total energy and event shape parameters.

The τ is a short-lived particle and every τ decay channel involves the production of a τ neutrino. This makes the total visible energy less useful as a cut parameter than it was

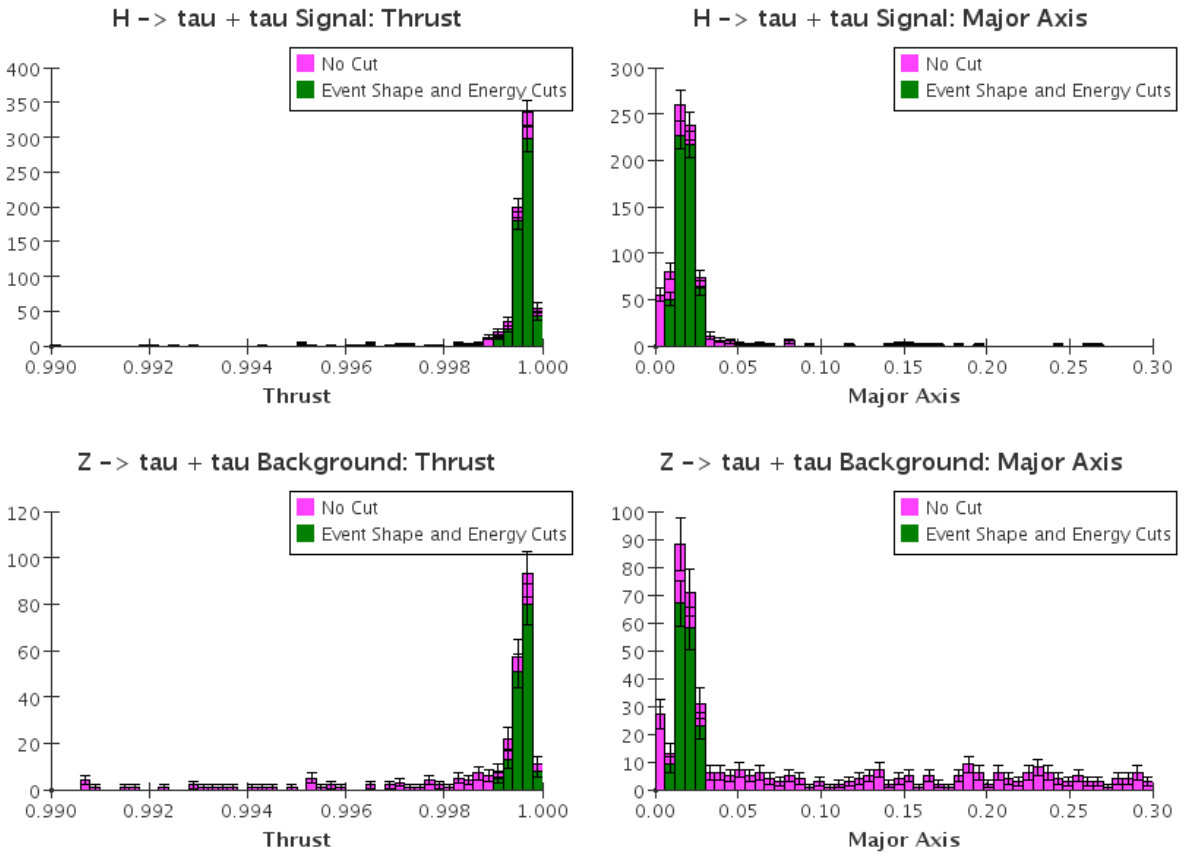

Figure 19: Effects of event shape and energy cuts on Higgs $\tau^+\tau^-$ signal and background. Cuts were made by selecting events with total energy $E_{tot} > 60.0GeV$ visible to the detector, thrust between 0.999 and 1.0 and major axis between 0.07 and 0.032. The signal is reduced to 78% and the background to 39%.

for $b\bar{b}$, since there are random amounts of missing energy. We require at least 60.0 GeV to be visible because background dominates below this value due to boosted Z's. Event shape parameters, however, are very useful here since τ decays typically do not create a widespread shower. We require the thrust to be between 0.999 and 1.0 and the major axis to be between 0.007 and 0.03. This cut reduces the signal to 78% of its original value and the background to 39%, bringing the Higgs cross section to 1.58 pb and the background to 4.97 pb, as seen in Figure 19. The cut is specific enough that it is not necessary to assume anything else about the events, such as a perfect $\tau^+\tau^-$ tag. Fewer than 0.2% of the Higgs decays that pass the cut are not $\tau^+\tau^-$ events and only 6.4% of the background events that pass are misidentified. The effective background cross section above is calculated from all the events which pass the cut. Plots of simulated data can be found in Appendix **??** and fitted values can be found in Table 10.

7.2.4 $H^0 \to \gamma\gamma$

The final channel examined in this report is the $H^0 \to \gamma\gamma$ channel. The Higgs branching fraction for this channel is only 0.3%, but the events can't be easily identified by selecting events with two photons with equal energy adding up to $\sqrt{s}$ and high thrust. About 10% of these events are lost when one or both photons hit the cone and there is no background so the cross section is 0.077 pb. The high purity of this channel is a great advantage, but the small cross section makes it impractical for scanning the beam energy to find the Higgs peak as it takes a great deal of luminosity to expect more than a few events on the peak. This channel will require much luminosity but may prove very useful for precise measurements of the Higgs.

7.3 Higgs Measurements

In the previous section we fit simulated data to extract the properties of the Higgs. While it is clear that the $b\bar{b}$ and WW^* channels will be the most useful for measuring Higgs properties, particularly with lower luminosities, the results of these fits are not reliable estimates of the achievable accuracy and precision of a muon collider. The values quoted were individual samples from trials that varied significantly in both accuracy and precision and which used the approximation that the background cross section, luminosity per point and beam resolution are well-known parameters. In this section we maintain this assumption and estimate the achievable accuracy and luminosity dependence of these

Channel	$\mu^+\mu^- \to H^0 \to X$			$\mu^+\mu^- \to Z\gamma^* \to X$			$S/\sqrt{B}$
	Br	σ (pb)		Br	σ (pb)		
Total	1.0	σ_s	28.3	1.0	σ_b	301.4	1.63
		σ_{eff}	22.4		σ_{eff}	126.4	1.99
$b\bar{b}$	0.584	σ_s	16.5	0.152	σ_b	57.2	2.18
		σ_{eff}	8.64		σ_{eff}	8.45	2.97
WW^*	0.226	σ_s	6.39	2e-4	σ_b	0.05	28.6
		σ_{eff}	3.35		σ_{eff}	0.05	15.0
$\tau^+\tau^-$	0.071	σ_s	2.01	0.034	σ_b	12.8	0.56
		σ_{eff}	1.58		σ_{eff}	4.97	0.71
$\gamma\gamma$	0.003	σ_s	0.077	—	σ_b	—	—
		σ_{eff}	—		σ_{eff}	—	—

Table 9: Branching fractions, cross sections before and after cuts and $S/\sqrt{B}$ for the channels studied.

Channel		$\Gamma_{H\to X}(MeV)$	$\Delta M_H(MeV)$	$Br(H^0 \to X)$
Total	Raw	4.56 ± 1.52	0.13 ± 0.16	0.96 ± 0.04
	Cut	5.57 ± 1.33	-0.02 ± 0.14	0.65 ± 0.01
$b\bar{b}$	Raw	3.49 ± 1.83	-0.06 ± 0.19	0.67 ± 0.05
	Cut	4.78 ± 0.48	0.01 ± 0.05	0.271 ± 0.001
WW^*	Raw	4.06 ± 0.24	0.00 ± 0.07	0.217 ± 0.001
	Cut	3.96 ± 0.17	-0.16 ± 0.04	0.1271 ± 0.0002
$\tau^+\tau^-$	Raw	4.82 ± 4.46	-0.54 ± 0.47	0.0623 ± 0.0005
	Cut	0.84 ± 2.97	1.07 ± 0.30	0.24 ± 0.23
$\gamma\gamma$	Raw	2.85 ± 5.73	-0.6 ± 0.9	0.0035 ± 0.0001
	Cut	—	—	—

Table 10: Fitted values of Higgs decay width, mass and branching ratio from simulated data. Mass values are the difference between the measured mass and the true mass of 126,000 MeV. Total integrated luminosity was 1 fb^{-1}, or 71.4pb^{-1} per data point.

measurements.

7.3.1 Measurements With the $b\bar{b}$ Channel

The uncertainties in the measured values do not always reflect the accuracies of the measurements or their statistical variance from experiment to experiment. To get a better estimation we repeated the experiment of simulating 1 fb^{-1} of data and fitting it forty times. Figure 20 shows the results of this in box-and-whisker plots for a range of integrated luminosities. To reiterate, each experiment simulates taking data in a 60 MeV range around the Higgs peak with 14 bins separated by the beam width of 4.2 MeV. The integrated luminosity is the sum of luminosity taken in each bin.

These plots demonstrate that our simplistic simulation and fitting experiment is on average accurate, but the statistical variance is high. While a more thorough analysis may provide more consistent results, we conclude here that at a given luminosity, the Higgs parameters can be measured to within the inner-quartile range given. At an integrated luminosity of 1 fb^{-1}, we can use the $b\bar{b}$ channel with energy and event shape cuts to accurately measure the mass of the Higgs to within 0.3 MeV, the partial width to within 0.9 MeV and the branching ratio to within 0.09.

7.3.2 Measurements with the WW^* Channel

We performed the same simulated experiments using our estimated cross sections for the WW^* channel and background, as shown in Figure 21. We find that with an integrated luminosity of 1 fb^{-1}, we can use the WW^* channel with a lepton and missing energy to accurately measure the mass of the Higgs to within 0.38 MeV, the partial width to within 0.75 MeV and the branching ratio to within 0.02. These values can be found in Table 11

7.4 Combining Channels

To measure the Higgs mass and total width more precisely, we took advantage of both channels. We did this by simulating data for both channels at the same time and taking their average, weighted by the uncertainty in the fits. For example, the formula used for the width was:

$$\delta\overline{\Gamma_H} = \frac{\delta\Gamma_{b\bar{b}}}{\delta\Gamma_{b\bar{b}} + \delta\Gamma_{WW^*}}\Gamma_{WW^*} + \frac{\delta\Gamma_{WW*}}{\delta\Gamma_{b\bar{b}} + \delta\Gamma_{WW^*}}\Gamma_{b\bar{b}} \tag{7.5}$$

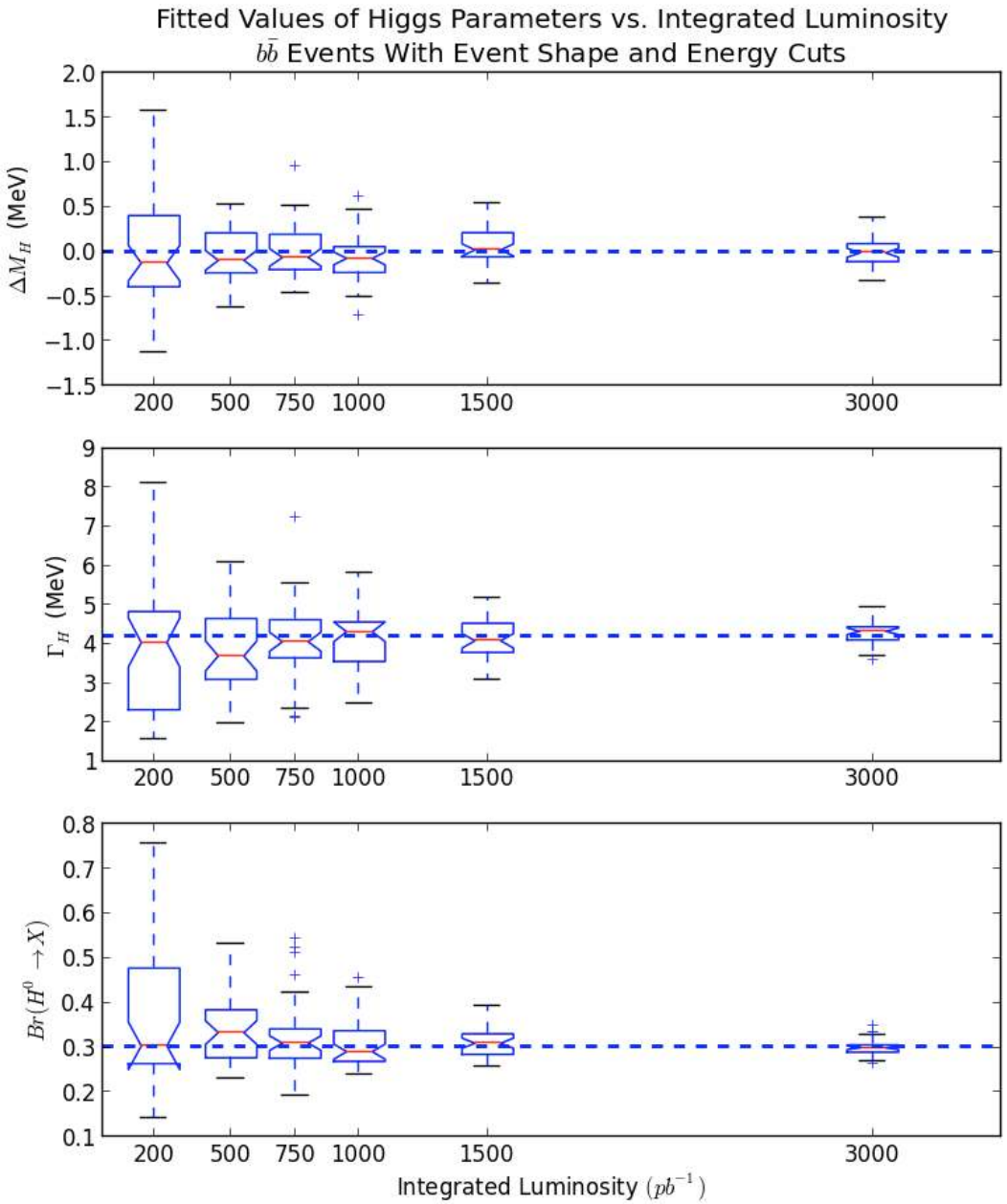

Figure 20: Box-and-whisker plots of fitted values of the Higgs mass, $b\bar{b}$ partial width and $b\bar{b}$ branching ratio for 40 experiments at each luminosity. Integrated luminosity is the total luminosity taken in 14 bins 4.2 MeV apart in a 60 MeV range centered on the Higgs mass. The boxes extend to the upper and lower quartiles of the data and the 'whiskers' extend to the most extreme value within 1.5 times the inner-quartile range.

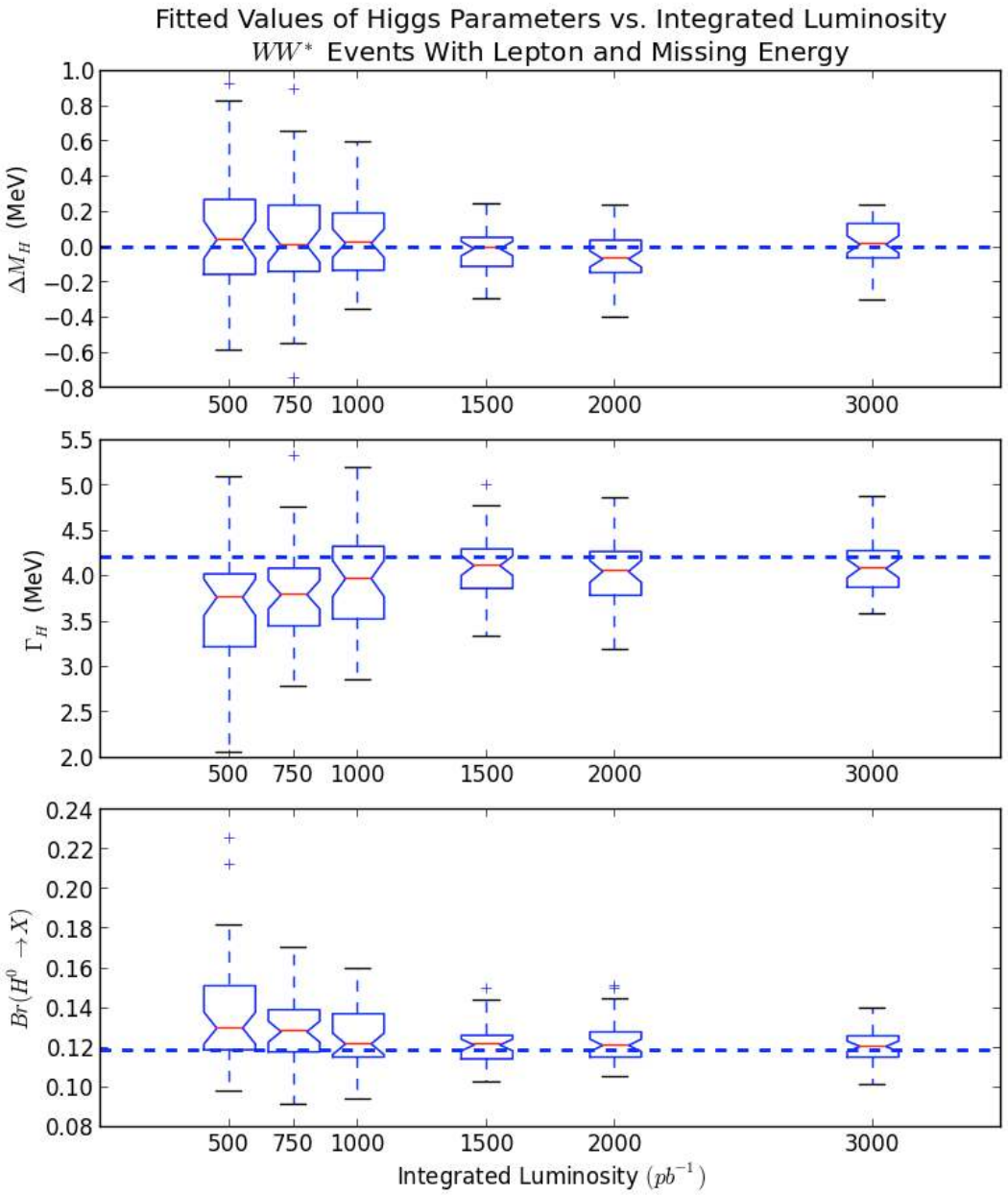

Figure 21: Box-and-whisker plots of fitted values of the Higgs mass, WW^* partial width, and WW^* branching ratio for 40 experiments at each luminosity. Integrated luminosity is the total luminosity taken in 14 bins 4.2 MeV apart in a 60 MeV range centered on the Higgs mass. The boxes extend to the upper and lower quartiles of the data and the 'whiskers' extend to the most extreme value within 1.5 times the inner-quartile range.

Channel	δM_H (MeV)	$\delta\Gamma_H$ (MeV)	$\delta Br(H^0 \to X)$
$b\bar{b}$	0.30	0.60	0.09
WW^*	0.40	0.75	0.02
Combined	0.25	0.45	—

Table 11: Accuracy of fitting parameters for simulated Higgs data. Values represent the inner quartile range (25% to 75%) of the values of 40 simulated experiments using 1 fb^{-1} total integrated luminosity. The combined values were calculated after each experiment using a weighted average.

As shown in Figure 22, the mass measurement was found to be accurate within 0.25 MeV and the total width was accurate within 0.45 MeV. All the estimated accuracies can be found in Table 11.

7.5 Discussion and Conclusion

The Higgs boson is a particle of fundamental importance to physics and measuring its properties with precision will allow us to probe the limits of the Standard Model and may point the way towards non-Standard model physics. Using simple estimates of physics backgrounds and separable signal we have estimated that with 1 fb^{-1} of integrated luminosity a hypothetical muon collider Higgs factory operating at the Higgs s-channel resonance could measure the mass of a Standard Model 126 GeV Higgs to within 0.25 MeV and its total width to within 0.45 MeV. We estimated that with a beam spread of 4.2 MeV, approximately 368 pb^{-1} total integrated luminosity would be required to guarantee locating the narrow Higgs peak. We believe that these preliminary results strongly motivate further research and development towards the construction of a muon collider Higgs factory.

Our estimations assume that there is no machine-induced background and that the detector has excellent tracking and calorimetry. Our results demonstrate the value of the high Higgs cross section and narrow beam energy spread available at a muon collider. These two factors enable the direct measurement of the Higgs mass and width by scanning the Higgs s-channel resonance, which is not possible at any e^+e^- collider. Our study of the physics-induced background and separation of the Higgs signal showed that significant reduction of the physics background can be achieved by a detector with high energy and spatial resolution. We believe that this report justifies more in-depth analysis of Higgs channels and their backgrounds, for example the reconstruction of $H^0 \to WW^* \to 4j$

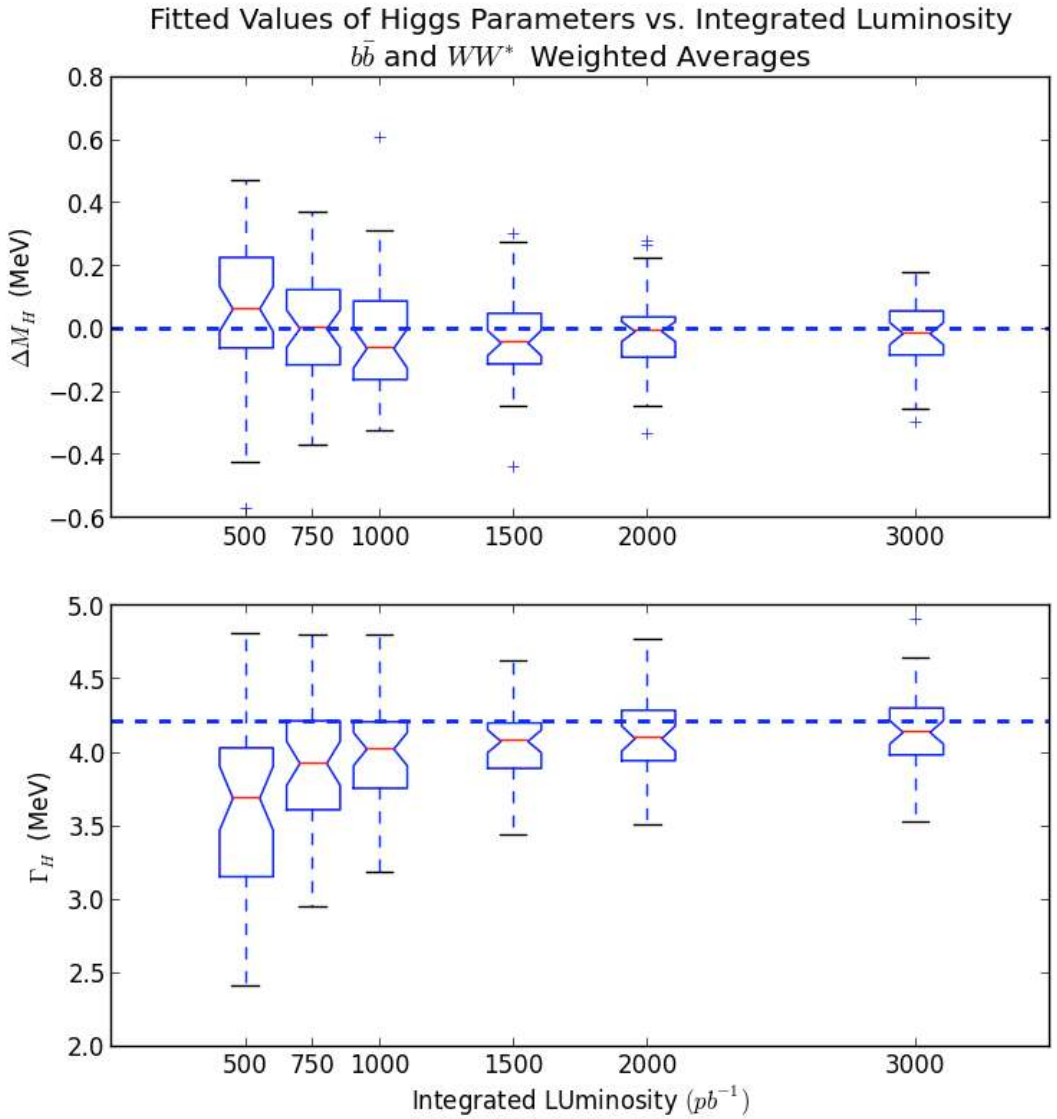

Figure 22: Box-and-whisker plots of fitted values of the Higgs mass and total width for 40 experiments at each luminosity. Integrated luminosity is the total luminosity taken in 14 bins 4.2 MeV apart in a 60 MeV range centered on the Higgs mass. The boxes extend to the upper and lower quartiles of the data and the 'whiskers' extend to the most extreme value within 1.5 times the inner-quartile range.

events using learning algorithms or the application of flavor-tagging techniques to tag $b\bar{b}$ events.

Machine-induced backgrounds, mainly from muon decays in the beam, present an additional difficulty which has not yet been studied in great detail. We believe that in addition to significant shielding in the detector cone and endcaps, it may be important to have a calorimeter with high spatial and temporal resolution. Our results motivate an in-depth analysis of the machine-induced background including simulation in a highly segmented, totally-active, dual readout calorimeter such as the MCDRCal01 detector concept.

References

[1] G. Aad *et al.* , ATLAS Collaboration, "Observation of a New Particle in the Search for the Standard Model Higgs Boson with the ATLAS Detector at the LHC," arXiv:1207.7214 [hep-ex], Phys. Lett. B716, 1 (2012);
Chatrchyan *et al.* , CMS Collaboration, "Observation of a new boson at a mass of 125 GeV with the CMS experiment at the LHC," arXiv:1207.7235 [hep-ex], Phys. Lett. B716, 30 (2012).

[2] S. Weinberg, Phys. Rev. Lett. **19**, 1264 (1967).

[3] D. Neuffer, "The First Muon Collider - 125 GeV Higgs Factory?," AIP Conf. Proc. **1507**, 849 (2012).

[4] Yuri Alexahin, UCLA Workshop, 2013, https://hepconf.physics.ucla.edu/higgs2013/talks/alexahin.pdf

[5] B. Grinstein, "Higgs, Higgs impostors, Higgs lookalikes and all that", Presented at the Higgs Factory Muon Collider Workshop at UCLA, March 21-23, 2013 (unpublished) [`https://hepconf.physics.ucla.edu/higgs2013/talks/grinstein.pdf`]

[6] J. Alwall, M. Herquet, F. Maltoni, O. Mattelaer and T. Stelzer, JHEP **1106**, 128 (2011) [arXiv:1106.0522 [hep-ph]].

[7] S. Dittmaier, S. Dittmaier, C. Mariotti, G. Passarino, R. Tanaka, S. Alekhin, J. Alwall and E. A. Bagnaschi *et al.*, arXiv:1201.3084 [hep-ph].

[8] T. Han and Z. Liu, Phys. Rev. D **87**, 033007 (2013) [arXiv:1210.7803 [hep-ph]].

[9] A. Conway and H. Wenzel, arXiv:1304.5270 [hep-ex].

[10] E. Eichten, "Physics at a Muon Collider Higgs Factory", Presented at the Higgs Factory Muon Collider Workshop at UCLA, March 21-23, 2013 (unpublished) [`https://hepconf.physics.ucla.edu/higgs2013/talks/eichten.pdf`]

[11] M. Purohit, "Can we observe $h^0 \to c\bar{c}$?", Presented at the Higgs Factory Muon Collider Workshop at UCLA, March 21-23, 2013 (unpublished) [`https://hepconf.physics.ucla.edu/higgs2013/talks/purohit.pdf`]

[12] A. Blondel, A. Chao, W. Chou, J. Gao, D. Schulte and K. Yokoya, arXiv:1302.3318 [physics.acc-ph].

[13] P. J. Clark [ATLAS Collaboration], EPJ Web Conf. **49**, 12011 (2013).

[14] T. Sjostrand, S. Mrenna and P. Z. Skands, Comput. Phys. Commun. **178**, 852 (2008) [arXiv:0710.3820 [hep-ph]].

[15] M. Duhrssen, S. Heinemeyer, H. Logan, D. Rainwater, G. Weiglein and D. Zeppenfeld, hep-ph/0407190.

[16] V. Barger, M. Ishida and W. -Y. Keung, Phys. Rev. Lett. **108**, 261801 (2012) [arXiv:1203.3456 [hep-ph]].

[17] P. M. Ferreira, H. E. Haber, R. Santos and J. P. Silva, arXiv:1211.3131 [hep-ph].

[18] A. Celis, V. Ilisie and A. Pich, arXiv:1302.4022 [hep-ph].

[19] A. Efrati, D. Grossman and Y. Hochberg, arXiv:1302.7215 [hep-ph].

[20] J. F. Gunion, Y. Jiang and S. Kraml, Phys. Rev. D **86**, 071702 (2012) [arXiv:1207.1545 [hep-ph]].

[21] D. G. Cerdeno, P. Ghosh and C. B. Park, arXiv:1301.1325 [hep-ph].

[22] N. D. Christensen, T. Han, Z. Liu and S. Su, arXiv:1303.2113 [hep-ph].

[23] Y. Grossman, Z. 'e. Surujon and J. Zupan, JHEP **1303**, 176 (2013) [arXiv:1301.0328 [hep-ph]].

[24] E. Eichten and A. Martin, arXiv:1306.2609 [hep-ph].

[25] R. Raja and A. Tollestrup, *Physical Review D* **58**, 013005 (1998).

[26] R. Raja and A. Tollestrup, AIP Conf. Proc. **435**, 583 (1998).

[27] A. Blondel, Energy calibration by spin precession in Prospective Study of Muon Storage Rings at CERN, (B. Autin, , A. Blondel and J. Ellis, ed.) CERN 99-02 (1999), pp. 51-54.

[28] A. Blondel, Muon Polarisation in the neutrino factory, NIM A451, 131-137 (2000).

[29] A. Para, talk given in International Linear Collider Workshop 2008 at Chicago.

[30] H. Wenzel, talk given at the 2009 Linear Collider Workshop of the Americas, Albuquerque, September 2009.

[31] The Dream Collaboration, R. Wigmans, Recent Results from the Dream Project, in Proceed- ings of XIII International Conference on Calorimetry in Particle Physics, Ed. M. Fraternali et al., IOP Conference Series Volume 160 (2009) 012018, and N. Akchurin et al., Nucl. Instr. and Meth. A582 (2007) 474, A584 (2008) 304, A593 (2008) 530, A595 (2008) 359 and A598 (2008) 710.

[32] http://cepa.fnal.gov/psm/stdhep/

[33] http://physics.uoregon.edu/ lc/alcpg/

[34] http://lcio.desy.de/

[35] http://www.lcsim.org/software/lcdd/

[36] The two main reference papers for Geant4 are published in Nuclear Instruments and Methods in Physics Research A 506 (2003) 250-303, and IEEE Transactions on Nuclear Science 53 No. 1 (2006) 270-278.
http://www.Geant4.org/Geant4/

[37] http://jas.freehep.org/jas3/

[38] http://www.lcsim.org/software/lcsim/

[39] http://wired.freehep.org/

[40] http://lcgapp.cern.ch/project/simu/framework/GDML/gdml.html

[41] T.J. Roberts and D. Kaplan, *G4beamline Simulation Program for Matter Dominated Beamlines",* Proc. of PAC07, p3468, also see [].

[42] Y. Alexahin et al., "Conceptual Design of the Muon Collider Ring Lattice", Proc. of IPAC'10, Kyoto (2010).
[`http://accelconf.web.cern.ch/AccelConf/IPAC10/papers/tupeb021.pdf`]

[43] Y. Alexahin et al., "Muon Collider Interaction Region Design", Proc. of IPAC'10, Kyoto, (2010).
[`http://accelconf.web.cern.ch/AccelConf/IPAC10/papers/tupeb022.pdf`]

[44] The SiD Detector is described at http://www.SiliconDetector.org

[45] O. Benary, S. Kahn, and I. Stumer, *Detector Backgrounds for a High Energy Muon Collider,* AIP Conf. Proc. **530** (2000), p1-12.

[46] The MARS Code System, http://www-ap.fnal.gov/MARS

[47] N.V. Mokhov, S.I. Striganov, *"Detector background at muon colliders"*, Fermilab-PUB-11-483-APC (2011).

[48] N.V. Mokhov, *"The Mars Code System User's Guide"*, Fermilab-FN-628 (1995); N.V. Mokhov, S.I. Striganov, *"MARS15 Overview"*, Proc. of Hadronic Shower Simulation Workshop, Fermilab,September 2006, AIP Conf. Proc. 896, pp 50-60 (2007).

[49] A. Mazzacane, *"Muon Collider Tracking Studies in ILCroot"*, Muon Collider 2011, Telluride, Colorado, [Telluride Talk] A. Mazzacane, *"Muon collider backgrounds"*, Snowmass 2013: Lepton Collider Workshop, 10-11 April 2013, MIT [MIT Talk]

[50] N. Terentiev, *"Simulation of the Tracker and Vertex Silicon Detector Hits Response to machine Backgrounds in a Muon Collider"*, Higgs Factory Muon Collider Workshop, UCLA, March 21-23, 2013,
[]

[51] C. Gatto, *"Muon Collider Detector Studies in ILCroot"*, International Workshop on Future Linear Colliders, Sep. 28, 2011, Granada, [Gatto talk]; V. Di Benedetto, *"Recent developments on ILCroot"*, May 18, 2011, Fermilab, [Di Benedetto talk]

[52] J. Chapman and S. Geer, *"The Pixel Microtelescope"*, FERMILAB-Conf-96/375

[53] R. Lipton, Talk given at Muon Collider Physics and Detector meeting, need a link to it

[54] M. Palmer, "Muon Accelerators: An Integrated Path to Intensity and Energy Frontier Physics Capabilities", Presented at the Higgs Factory Muon Collider Workshop at UCLA, March 21-23, 2013 (unpublished)
[`https://hepconf.physics.ucla.edu/higgs2013/talks/palmer.pdf`]

[55] T. Muller, "The Higgs Boson: Latest Measurements", Presented at the Higgs Factory Muon Collider Workshop at UCLA, March 21-23, 2013 (unpublished)
[`https://hepconf.physics.ucla.edu/higgs2013/talks/tmuller.pdf`]

[56] J.P. Delahaye, "Higgs Factory: Overview of Technology Options", Presented at the Higgs Factory Muon Collider Workshop at UCLA, March 21-23, 2013 (unpublished)
[`https://hepconf.physics.ucla.edu/higgs2013/talks/delahaye.pdf`]